Jefferson Lab PAC24
Proposal Cover Sheet

This document must be received by close of business Monday,

April 28,2003 at:

Jefferson Lab
User/International Liaison
Mail Stop 12B
12000 Jefferson Ave.
Newport News, VA
23606

Experimental Hall: Hall A

Days Requested for Approval: 25

❒ **Proposal Title:**

Deeply Virtual Compton Scattering on the Neutron

Proposal Physics Goals

Indicate any experiments that have physics goals similar to those in your proposal.

Approved, Conditionally Approved, and/or Deferred Experiment(s) or proposals:

Contact Person

Name: Franck Sabatié
Institution: DAPNIA/SPhN
Address: CEA/Saclay
Address:
City, State, ZIP/Country: F91191, Gif sur Yvette, France
Phone: + 33 169 08 32 06 **Fax:** + 33 169 08 75 84
E-Mail: sabatie@jlab.org

Jefferson Lab Use Only

Receipt Date:_____

By:_____

BEAM REQUIREMENTS LIST

JLab Proposal No.: _____ Date: _____

Hall: Hall A Anticipated Run Date: _____ PAC Approved Days: _____

Spokesperson: P. Bertin, C.E. Hyde-Wright, F. Sabatié, E. Voutier Hall Liaison: _____
Phone: x7544, x7544, x7544, x6932
E-mail: bertin@jlab.org, hyde@jlab.org, sabatie@jlab.org, voutier@jlab.org

List all combinations of anticipated targets and beam conditions required to execute the experiment. (This list will form the primary basis for the Radiation Safety Assesment Document (RSAD) calculations that must be performed for each experiment.)

Condition No.	Beam Energy (MeV)	Mean Beam Current (μA)	Polarization and Other Special Requirements (e.g., time structure)	Target Material (use multiple rows for complex targets — e.g., w/windows)	Material Thickness (mg/cm^2)	Est. Beam-On Time for Cond. No. (hours)
1	6.0	4.2	80% polarization	15cm LD2	2535	600
				2x100μm Al	54	600

The beam energies, E_{Beam}, available are: $E_{Beam} = N \times E_{Linac}$ where N = 1, 2, 3, 4, or 5. E_{Linac} = 800 MeV, i.e., available E_{Beam} are 800, 1600, 2400, 3200, and 4000 MeV. Other energies should be arranged with the Hall Leader before listing.

HAZARD IDENTIFICATION CHECKLIST

JLab Proposal No.: _____ Date: _____
(For CEBAF User Liaison Office use only.)

Check all items for which there is an anticipated need.

Cryogenics
- X beamline magnets
- X analysis magnets
- X target
  - type: LD2 15cm standard
  - flow rate: standard
  - capacity: standard

Electrical Equipment
- _____ cryo/electrical devices
- _____ capacitor banks
- _____ high voltage
- _____ exposed equipment

Radioactive/Hazardous Materials
List any radioactive or hazadorous/ toxic materials planned for use:
_____
_____
_____
_____

Pressure Vessels
- _____ inside diameter
- _____ operating pressure
- _____ window material
- _____ window thickness

Flammable Gas or Liquids
- type: LD2
- flow rate: -
- capacity: 5g

Drift Chambers
- type: _____
- flow rate: _____
- capacity: _____

Other Target Materials
- ___ Beryllium (Be)
- ___ Lithium (Li)
- ___ Mercury (Hg)
- ___ Lead (Pb)
- ___ Tungsten (W)
- ___ Uranium (U)
- ___ Other (list below)

_____
_____

Vacuum Vessels
- _____ inside diameter
- _____ operating pressure
- _____ window material
- _____ window thickness

Radioactive Sources
- _____ permanent installation
- _____ temporary use
- type: _____
- strength: _____

Large Mech. Structure/System
- X lifting devices
- _____ motion controllers
- _____ scaffolding or
- X elevated platforms

Lasers
- type: _____
- wattage: _____
- class: _____

Installation:
- _____ permanent
- _____ temporary

Use:
- _____ calibration
- _____ alignment

Hazardous Materials
- ____ cyanide plating materials
- ____ scintillation oil (from)
- ____ PCBs
- ____ methane
- ____ TMAE
- ____ TEA
- ____ photographic developers
- ____ other (list below)

_____
_____

General:

Experiment Class:

- _____ Base Equipment
- X Temp. Mod. to Base Equip.
- _____ Permanent Mod. to Base Equipment
- X Major New Apparatus

Other: _____
_____

LAB RESOURCES LIST

JLab Proposal No.: _____ Date _____
(For JLab ULO use only.)

List below significant resources — both equipment and human — that you are requesting from Jefferson Lab in support of mounting and executing the proposed experiment. Do not include items that will be routinely supplied to all running experiments such as the base equipment for the hall and technical support for routine operation, installation, and maintenance.

Major Installations *(either your equip. or new equip. requested from JLab)*

Installation of DVCS scattering chamber as defined in experiment E00-110, installation of proton array and calorimeter platform and DVCS/BigBite stand as defined in the same experiment.

Please take the E00-110 requirements as the base requirements for this proposal/experiment.

New Support Structures: _____

Data Acquisition/Reduction

Computing Resources: _____

New Software: _____

Major Equipment

Magnets: _____

Power Supplies: _____

Targets: _____

Detectors: New tagger system which is held by the same support system as the proton array

Electronics: _____

Computer Hardware: _____

Other: _____

Other: _____

Computing Requirements List

Proposal Title: Deeply Virtual Compton Scattering on the Neutron

Spokesperson: P. Bertin, C.E. Hyde-Wright, F. Sabatié, E. Voutier **Experimental Hall:** Hall A

Raw Data Expected

Total: 2 TB **Per Year (long duration experiments only):** _____

Simulation Compute Power (SPECint95 hours) Required: _____

On-Line Disk Storage Required: 100 GB

Imported Data Amount from Outside Institutions: _____

Exported Data Amount to Outside Institutions:w _____

Expected Mechanism for Imported/Exported Data: _____

Special Requirements

For example, special configuration of data acquisition systems) that may require resources and/or coordination with JLab's Computer Center. Please indicate, if possible, what fraction of these resources will be provided by collaborating institutions and how much is expected to be provided by JLab.

Proposal to Jefferson Lab PAC 24

Deeply Virtual Compton Scattering On The Neutron

P. Bertin (co-spokesperson), A. Camsonne, C. Ferdi, G. Lavessière and G. Smirnov
University Blaise Pascal/IN2P3

F. Sabatié (co-spokesperson and contact person), M. Garçon and C. Muñoz Camacho
DSM/DAPNIA/SPhN CEA Saclay

E. Voutier (co-spokesperson), C. Furget, S. Kox, G. Quéméner and J.-S. Réal
LPSC Grenoble/IN2P3

C. E. Hyde-Wright (co-spokesperson), D. Hayes and L. Weinstein
Old Dominion University

J.-P. Chen, E. Chudakov, R. Feuerbach, J. Gomez, O. Hansen, D. Higinbotham, K. de Jager, J. LeRose, R. Michael, S. Nanda, B. Reitz, J. Roche, A. Saha and B. Wojtsekhowski
Jefferson Laboratory

P. Markowitz
Florida International University

A. M. Nathan
University of Illinois at Urbana-Champaign

M. Vanderhaeghen
Institut für Kernphysik, University Mainz

M. Guidal
IPN Orsay/IN2P3

K. McCormick, X. Jiang and R. Ransome
Rutgers University

P. Solvignon
Temple University

A. Deur and N. Liyanage
University of Virginia

A. Voskanian
Yerevan Physics Institute

and

The Hall A Collaboration

(April 28, 2003)

Abstract

The Generalized Parton Distribution (GPD) universe has just been tackled by recent measurements which have confirmed that Deeply Virtual Compton Scattering (DVCS) experiments can be achieved at existing facilities and especially Jefferson Lab at moderate Q^2. Experiments E00-110 in Hall A and E01-113 in Hall B will extract the helicity dependent DVCS cross-sections and asymmetries on the proton in the Q^2 range 1.5-3.5 GeV^2. However, proton experiments can only constrain or extract the H and $\widetilde{H}$ GPDs because of the specific weighting in the asymmetry observable. A neutron DVCS experiment will be mostly sensitive to the least known of GPDs: E. It is essential to access the E GPD not only because it is one of the ingredients in our understanding of the nucleon structure, but also because it enters on equal footings with H in Ji's sum rule, relating H and E to the total angular momentum carried by quarks in the nucleon. Moreover, current GPD models constrain E by a parametrization using fractions of angular momentum carried by the u and d quarks in the nucleon. A comparison of the neutron DVCS single spin asymmetry with these models will yield interesting insights on the nucleon orbital momentum even though Ji's sum rule cannot be accessed with current facilities.

We propose to measure the DVCS beam-helicity dependent cross-sections and asymmetry on the neutron, at fixed $Q^2 = 1.9$ GeV^2 for two values of $x_B = 0.31$ and 0.36. We will use the polarized beam on the 15 cm liquid deuterium target and will detect the scattered electron in the left HRS, the emitted photon in a PbF_2 calorimeter and the recoil neutron in a scintillator array. In addition to the Hall A DVCS equipment in construction for the proton experiment E00-110, we will add shielding and a charged particle tagger (ΔE veto) in front of the scintillator array. With this modification, we will be able to measure $D(e, e'n\gamma)p$ events, and veto the $D(e, e'p\gamma)n$ events which penetrate the shielding. Each kinematical setting will require 300 hours of 6 GeV, 4.2μA beam at 80% polarization.

1 Introduction

The electromagnetic structure of the nucleon has been studied during the past five decades through measurements of form factors using elastic scattering and structure functions using deep inelastic scattering (DIS) [1, 2, 3, 4, 5, 6]. However, despite a large number of experimental results, the nucleon is still not understood: form factors and structure functions are but one-dimensional pictures taken under two different angles of a very complicated object. Straightforwardly, since one probes the same object with both experiments, the pictures taken under different angles must be connected at some level. The Generalized Parton Distribution (GPD) framework introduced 6 years ago allows one to have a unified description of the nucleon, including form factors and structure functions, but also including two-parton correlations and transverse momentum dependence. The GPDs can therefore give three-dimensional pictures of the nucleon, giving information such as the transverse spatial dependence as a function of the longitudinal momentum fraction of quarks [7]. With a complete knowledge of these functions, it will be possible to locate for instance the high and low momentum components of the nucleon, even as a function of flavor. Note that the initial motivation for measuring GPDs was the determination of Ji's sum rule, relating the second moment of the sum of two GPDs to the total angular momentum carried by quarks in the nucleon.

Deeply Virtual Compton Scattering (DVCS) is the simplest process which can be described in terms of GPDs. It is the first reaction which will allow unambiguous extraction of GPDs from data, and is the cornerstone of their initial exploration at Jefferson Lab at 6 and 12 GeV. First results of DVCS asymmetries in Hall B and HERMES [8] suggest that the GPD framework is likely applicable to 6 GeV experiments. Using this beam energy, it is therefore desirable to understand as much as possible of the GPDs. Especially, we realized rather early on that there is potentially tremendous interest in extending these measurements using a liquid deuterium target since they are highly relevant to reach new information on the Generalized Parton Distributions.

We propose to measure the neutron helicity-dependent DVCS cross-sections and asymmetry at fixed $Q^2 = 1.9$ GeV^2 for two different Bjorken x. DVCS on the neutron is complementary to the proton case since it is very sensitive to the least known of GPDs which in addition, cannot be constrained by measurements on the proton. This GPD is especially important since it enters directly into Ji's sum rule.

DVCS on the neutron will use an improved version of the proton E00-110 experimental setup. Firstly, we will use the liquid deuterium target as a quasi-free neutron target. Secondly, since the DVCS reaction can either occur on the proton or neutron with exactly the same kinematics, we have planned to add a tagger system to the scintillator array to be able to discriminate between protons and neutrons. As with the proton experiment, the scattered electrons will be detected in the left HRS and the emitted photon in a dedicated PbF_2 calorimeter.

As this proposal is just an extension of the E00-110 experiment [9] to the neutron, the reader might find that the previous proposal contains more detailed information about part of the discussion, such as a more rigorous introduction to the physics of GPDs.

The next section will give a brief overview of the physics related to GPDs and will then focus on our motivations to perform a neutron DVCS measurement. Section 3 will describe our experimental strategy, including the description of the DVCS setup with the new tagger system, the chosen kinematics and expected results, but will also describe the issues with such an experiment and how we plan to handle them. Finally, the beam request will be described in the last section after a brief summary.

2 Theory and motivation

2.1 Generalized Parton Distributions: a brief overview

In the last 6 years or so, Ji, Radyushkin and others have shown that the DVCS reaction $\gamma^* N \to \gamma N$, in the Bjorken limit, can be factorized into a hard scattering kernel and a non-perturbative nucleon

structure part [10]. This is represented in Fig. 1, where the virtual photon scatters on a single quark line, which almost instantly re-emits a real photon. The quark is then "inserted back" into the nucleon, all of this happening in a very small amount of time. In kinematical terms, this factorization is valid when the virtual photon mass is large (large Q^2: one probes distances much smaller than the nucleon size) but the transfer to the proton is small compared to this scale ($-t << Q^2$: one leaves the proton almost unchanged overall). The soft structure of the nucleon is parameterized by four structure functions known as the GPDs: E, H, $\widetilde{E}$ and $\widetilde{H}$.

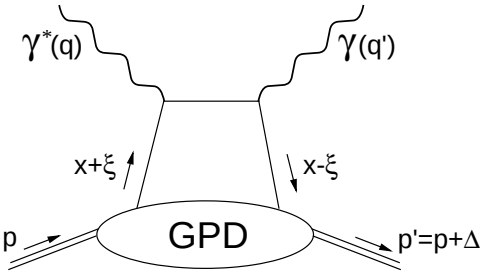

Figure 1: Handbag diagram to the DVCS process. x characterizes the light-cone momentum fraction of the struck quark in the loop. ξ is the longitudinal momentum fraction of the transfer to the proton $\Delta = p' - p$.

All four GPDs depend on 3 variables x, ξ and t: x characterizes the light-cone momentum fraction of the struck quark in the loop (which is not directly accessible experimentally). ξ is the longitudinal momentum fraction of the transfer to the proton $\Delta = p' - p$. It reduces to $\xi = x_B/(2 - x_B)$ at the Bjorken limit ($Q^2 \to \infty$). Finally, $t = \Delta^2$ is the standard Mandelstam variable representing the momentum transfer between the virtual and real photons.

In the forward direction ($\xi = t = 0$), the GPDs H and $\widetilde{H}$ reduce to the usual parton distributions $q(x)$ and $\Delta q(x)$:

$$H^q(x, \xi = 0, t = 0) = q(x)\,, \tag{1}$$

$$\widetilde{H}^q(x, \xi = 0, t = 0) = \Delta q(x)\,, \tag{2}$$

where q stands for the quark flavor. The first moments of the GPDs and the elastic form factors are related by the following relations:

$$\int_{-1}^{+1} dx H^q(x, \xi, t) = F_1^q(t)\,, \quad \int_{-1}^{+1} dx E^q(x, \xi, t) = F_2^q(t)\,, \tag{3}$$

$$\int_{-1}^{+1} dx \widetilde{H}^q(x, \xi, t) = g_A^q(t)\,, \quad \int_{-1}^{+1} dx \widetilde{E}^q(x, \xi, t) = h_A^q(t)\,, \tag{4}$$

where F_1^q and F_2^q are the Dirac and Pauli form factors, g_A^q is the axial form factor and h_A^q is the induced pseudoscalar form factor. Note that the ξ dependence drops out in the previous equations.

The second moment of the GPDs is relevant to the nucleon spin structure. It was shown in Ref. [11] that there exists a gauge-invariant decomposition of the nucleon spin:

$$\frac{1}{2} = J_q + J_g\,, \tag{5}$$

where J_q and J_g are respectively the total quark and gluon angular momentum contributions to the nucleon spin. J_q can be decomposed in a spin part $\Delta\Sigma$ and an orbital momentum part L_q as follows:

$$J_q = \frac{1}{2}\Delta\Sigma + L_q\,. \tag{6}$$

The second moment of the GPDs and the total angular momentum carried by quarks are related via Ji's sum rule:

$$\frac{1}{2}\int_{-1}^{+1} dx\, x[H(x,\xi,t=0)+E(x,\xi,t=0)] = J_q\,. \tag{7}$$

One should remember that $\Delta\Sigma$ is constrained in DIS experiments. Therefore, if one makes enough measurements to extract the second moments of the GPDs, the sum rule will determine the quark orbital momentum contribution to the nucleon spin. Of course, the measurement of J_q is beyond the scope of this proposal. Much more comprehensive information on Eq. 7 will be obtained with the 12 GeV upgrade to Jefferson Lab, and can be obtained with a new generation of facilities, including ELFE or an Electron-Ion Collider.

2.2 The DVCS asymmetry to access GPDs

The $eN \to eN\gamma$ process can either occur by radiation along one of the electron lines (Bethe-Heitler) or by emission of a real photon by the nucleon (DVCS) as shown in Fig. 2. The total cross-section is given by [12]:

$$\frac{d\sigma^{lN\to lN\gamma}}{dx_B dy d\Delta^2 d\varphi} = \frac{\alpha^3 x_B y}{16\pi^2 Q^2\sqrt{1+\epsilon^2}}\left|\frac{\mathcal{T}_{BH}+\mathcal{T}_{DVCS}}{e^3}\right|^2 \tag{8}$$

where $\epsilon = 2x_B M/Q$ and $\mathcal{T}_{DVCS}$ and $\mathcal{T}_{BH}$ are the amplitudes for the DVCS and Bethe-Heitler processes. φ is the angle between the leptonic plane (e,e') and the photonic plane (γ^*,γ). Since the BH process is completely calculable in QED (form factors at $t \sim 0.4$ GeV^2 are rather well known), the interference between the DVCS and the BH processes allows one to measure the real and imaginary part of the DVCS amplitude independently [13].

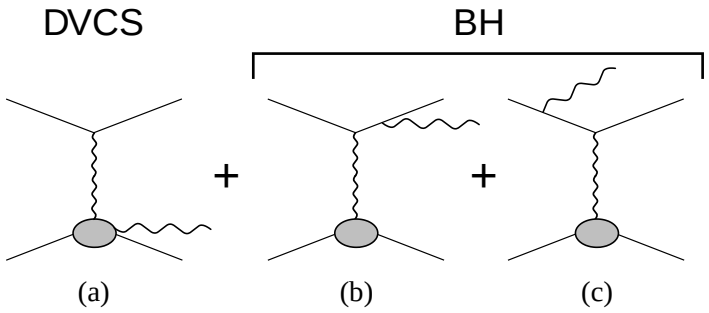

Figure 2: Diagrams contributing to the electroproduction of a real photon. The DVCS process (a) is shown along with the interfering Bethe-Heitler diagrams (b) and (c).

The specific observable we propose to measure is the cross-section difference for leptons of opposite helicities as a function of φ [14]. This observable is non-zero only if the emitted photon is out of the electron scattering plane ($\sin\varphi \neq 0$). This cross-section difference is proportional to the interference of the imaginary part of the DVCS amplitude with a known BH weight. The full expression for the difference in the cross-section for leptons of opposite helicities is given by [12]:

$$\frac{d\,\overrightarrow{\sigma}}{dx_B dy d\Delta^2 d\varphi} - \frac{d\,\overleftarrow{\sigma}}{dx_B dy d\Delta^2 d\varphi} = \Gamma(x_B,y,\Delta^2,\varphi)\cdot(A\sin\varphi + B\sin 2\varphi)\ . \tag{9}$$

The φ dependence of $\Gamma(x_B,y,\Delta^2,\varphi)$ originates from the electron propagators of the BH process. $\Gamma(x_B,y,\Delta^2,\varphi)$ can be written as:

$$\Gamma(x_B,y,\Delta^2,\varphi) = \frac{\alpha^3}{8\pi Q^2\sqrt{1+\epsilon^2}}\cdot\frac{1}{y\Delta^2\mathcal{P}_1(\varphi)\mathcal{P}_2(\varphi)}\cdot 8K\cdot(2-y)\,, \tag{10}$$

where the BH propagators can be written as:

$$Q^2\mathcal{P}_1 = (k-q')^2, \qquad Q^2\mathcal{P}_2 = (k-\Delta)^2 \ , \tag{11}$$

and where K is given by:

$$K^2 = \frac{-\Delta^2(1-y)}{Q^2} \cdot \left(1-y-\frac{y^2\epsilon^2}{4}\right)\cdot\left(1-\frac{\Delta^2_{min}}{\Delta^2}\right) \cdot \left(\sqrt{1+\epsilon^2}+\frac{4x_B(1-x_B)+\epsilon^2}{4(1-x_B)}\cdot\frac{\Delta^2-\Delta^2_{min}}{Q^2}\right) \ . \tag{12}$$

Having properly removed this BH φ-dependence in the cross-section along with the other kinematical dependencies, we will be left with a simple structure $A\sin\varphi + B\sin 2\varphi$. At leading twist, this asymmetry reduces to the $\sin\varphi$ term for which the coefficient is directly linked to the GPDs H, E and $\widetilde{H}$ through the following relation:

$$A = F_1(t)\mathcal{H} + \frac{x_B}{2-x_B}\cdot(F_1(t)+F_2(t))\cdot\widetilde{\mathcal{H}} - \frac{t}{4M^2}F_2(t)\mathcal{E} \ , \tag{13}$$

where $F_1(t)$ and $F_2(t)$ are the Dirac and Pauli form factors. $\mathcal{H}$, $\mathcal{E}$ and $\widetilde{\mathcal{H}}$ are given by

$$\mathcal{H} = \pi\sum_q e_q^2(H^q(\xi,\xi,t) - H^q(-\xi,\xi,t)) \tag{14}$$

$$\mathcal{E} = \pi\sum_q e_q^2(E^q(\xi,\xi,t) - E^q(-\xi,\xi,t)) \tag{15}$$

$$\widetilde{\mathcal{H}} = \pi\sum_q e_q^2(\widetilde{H}^q(\xi,\xi,t) + \widetilde{H}^q(-\xi,\xi,t)) \ . \tag{16}$$

The summations over $x=\xi$ and $x=-\xi$ in the previous expressions correspond to summations over quarks and antiquarks. In the case of the neutron in the *valence* region (neglecting the anti-quark contribution for simplification), this can be rewritten as:

$$\mathcal{H} = \pi\left(\frac{1}{9}H^u + \frac{4}{9}H^d\right) \tag{17}$$

$$\mathcal{E} = \pi\left(\frac{1}{9}E^u + \frac{4}{9}E^d\right) \tag{18}$$

$$\widetilde{\mathcal{H}} = \pi\left(\frac{1}{9}\widetilde{H}^u + \frac{4}{9}\widetilde{H}^d\right) \ . \tag{19}$$

The cross-section difference can be directly related to GPDs but its measurement is more complicated than trying to access the traditional relative asymmetry or single spin asymmetry (SSA) simply defined as:

$$SSA = \frac{\frac{d\vec{\sigma}}{dx_B dy d\Delta^2 d\varphi} - \frac{d\overleftarrow{\sigma}}{dx_B dy d\Delta^2 d\varphi}}{\frac{d\vec{\sigma}}{dx_B dy d\Delta^2 d\varphi} + \frac{d\overleftarrow{\sigma}}{dx_B dy d\Delta^2 d\varphi}} \ . \tag{20}$$

Indeed, the normalization, the efficiency and the acceptance factors cancel out in the ratio. It is clearly the simplest observable one can extract from the data but one can only rely on comparison with models to get information about GPDs: the SSA denominator (*i.e.* the total cross-section) contains φ-dependent terms and therefore does not simply decompose into $A\sin\varphi + B\sin 2\varphi$.

2.3 Particularities of DVCS on the neutron

The obvious interest in a neutron DVCS measurement - allowing a flavor decomposition of GPDs - is not what drives making such a difficult experiment. Actually, performing such a flavor decomposition

is a tricky task since the factors in front of the different GPD components in Eq. 13 change with the target. It is therefore not as trivial as simply extracting u and d components of structure functions. One will have to rely on models to achieve the flavor decomposition of the GPDs, but measurements on the neutron, being more sensitive to the d quark component, are mandatory.

Let us now emphasize why there is more to the neutron DVCS measurement than the flavor decomposition. Since equation 13 is essential to this discussion, let us write it here again:

$$A = F_1(t)\mathcal{H} + \frac{x_B}{2-x_B} \cdot (F_1(t) + F_2(t)) \cdot \widetilde{\mathcal{H}} - \frac{t}{4M^2} F_2(t)\mathcal{E} \ .$$

In the proton case, the leading term in the asymmetry's amplitude A is $F_1(t)\mathcal{H}$. Indeed, $F_1(t)$ and $\mathcal{H}$ are large for the proton, unlike $F_2(t)$, $\widetilde{\mathcal{H}}$ and $\mathcal{E}$ which turn out to be much smaller. The study of DVCS on the proton mostly gives us constraints on $\mathcal{H}$.

On the neutron, the exchange of the u and d quarks is not as straightforward as one would think: the $F_1(t)$ form factor is much smaller than $F_2(t)$, unlike in the proton's case [1]. The leading term in Eq. 13 becomes $-t/(4M^2) \cdot F_2(t)\mathcal{E}$ since $\widetilde{\mathcal{H}}$ is small by compensation of the u and d quarks contributions in the neutron case. The same effects makes the structure function g_1^n five times smaller than g_1^p at $x_B \simeq 0.3$. The neutron DVCS asymmetry is therefore dominated by the GPD E as shown in Table 1 and Table 2. In currently available models, E is the least known of the GPDs accessible using DVCS. By contrast, H and $\widetilde{H}$ are constrained by parton distributions which are well measured quantities. Furthermore, E and H enter on equal footings in Ji's sum rule. The knowledge of both GPDs is necessary to access the total angular momentum carried by quarks in the nucleon.

t	$F_2^n(t)$	$F_1^n(t)$	$(F_1^n(t) + F_2^n(t)) \cdot \xi$	$(-t/4M^2) \cdot F_2^n(t)$
-0.1	-1.46	-0.007	-0.27	-0.041
-0.3	-0.91	-0.038	-0.17	-0.077
-0.5	-0.60	-0.053	-0.12	-0.086
-0.7	-0.43	-0.059	-0.09	-0.084

Table 1: Values of the Pauli and Dirac form factors of the neutron as a function of t (within a given parametrization). The last 3 columns are the coefficients in front of the $\mathcal{H}$, $\widetilde{\mathcal{H}}$ and $\mathcal{E}$ terms respectively in Eq. 13. Note that since $\widetilde{\mathcal{H}}$ is small for the neutron, the asymmetry is dominated by $\mathcal{E}$.

Target	$\mathcal{H}$	$\widetilde{\mathcal{H}}$	$\mathcal{E}$
proton	1.13	0.70	0.98
neutron	0.81	-0.07	1.73

Table 2: $\mathcal{H}$, $\widetilde{\mathcal{H}}$ and $\mathcal{E}$ evaluated at $Q^2 = 2$ GeV^2, $x_B = 0.3$ and $-t$=0.3 GeV^2 using [15]. $\widetilde{\mathcal{H}}$ is small for the neutron compared to the proton due to a cancellation between the u and d quark contributions. $\mathcal{H}$ is smaller on the neutron than on the proton, and is multiplied by $F_1^n(t)$ in the expression of the $\sin\varphi$ term in the asymmetry which makes E the dominating GPD for this specific observable on the neutron.

The neutron DVCS experiment is complementary to the proton's. With both experiments, one will have the first accurate handle on the three GPDs H, $\widetilde{H}$ **and even** E **which is basically unknown and unconstrained**.

[1] Note that these form factors come from the Bethe-Heitler diagrams and as such, do not depend on Q^2 but on t which is much smaller.

2.4 Cross-section and asymmetry

We have estimated the cross-section and the asymmetry for a particular kinematics [15]: $Q^2 = 1.9$ GeV^2, $x_B = 0.31$. Fig. 3 shows the comparison of the proton and neutron cross-sections for this kinematics at $\varphi = 0$. At $\theta_{\gamma^*\gamma}$ close to zero, the neutron cross-section is about a factor 3 smaller than the proton cross-section.

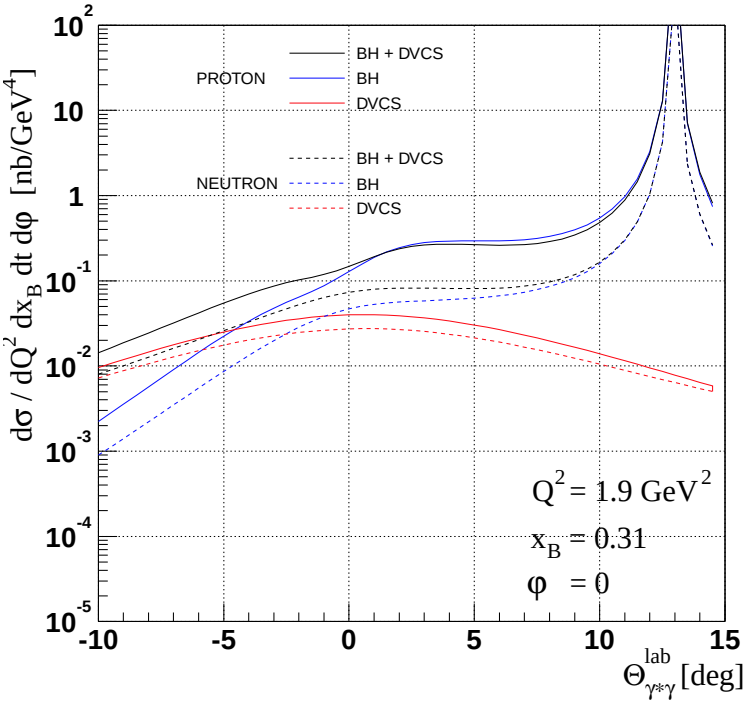

Figure 3: Neutron and proton cross-sections as a function of the angle between the virtual and real photons in the lab $\theta_{\gamma^*\gamma}$. Kinematics is $Q^2 = 1.9$ GeV^2, $x_B = 0.31$ and $\varphi = 0$. The contributions from the Bethe-Heitler process, the DVCS process and the total cross-sections are plotted for a *free* proton and neutron target [15].

The single spin asymmetry is represented in Fig. 4 for different parameters for the GPD E. As can be seen, the asymmetry can be as high as ≈10%. **Note that the GPD E is mostly unconstrained, therefore any variation in the parameters for the GPD E in a particular model results in a large relative variation in the beam-helicity dependent cross-sections and asymmetry**. The model we have used to evaluate the single spin asymmetry parametrizes E using J_u and J_d through Ji's sum rule [15] where J_u and J_d are the fractions of angular momentum carried by the u and d quarks in the proton. The comparison to this model can give us a great handle on the determination of J_u and J_d within this parametrization. The cross-section difference divided by $\Gamma(x_B, y, \Delta^2, \phi)$ as defined in Eq. 10 is shown in Fig. 5.

3 Experimental strategy

The extension of the E00-110 experiment will make use of the regular DVCS setup [9]. The neutron detection and the proton/neutron discrimination will be achieved by the addition of a tagger system. Extra shielding will not only help in the particle identification, but will also allow us to run at higher luminosity to compensate for the neutron efficiency and lower cross-section than in the proton case.

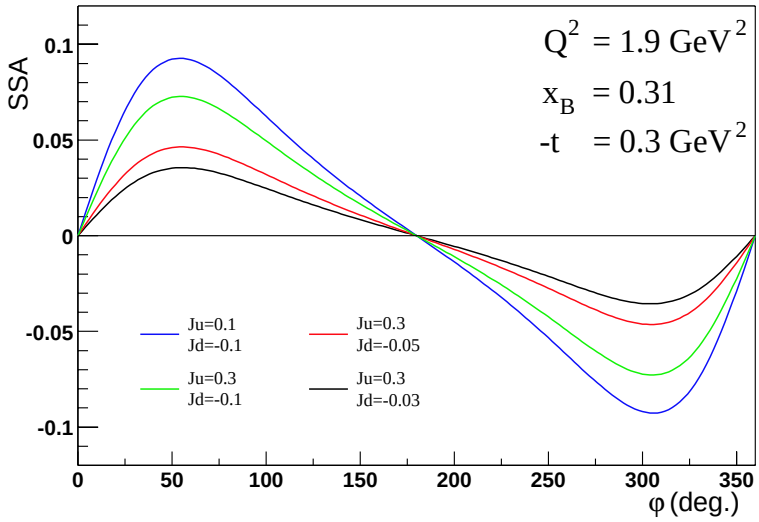

Figure 4: Neutron DVCS single spin asymmetry evaluated at $Q^2 = 1.9$ GeV^2, $x_B = 0.31$ and $-t = 0.3$ GeV^2 as a function of the azimuthal angle φ for different values of the parameters J_u and J_d within one model. J_u and J_d are the fractions of angular momentum carried by the u and d quarks in the proton which enter in Ji's sum rule. The only constraints to the GPD E comes from these parameters through Ji's sum rule, but they are totally unknown [15]. Note that the curves have been computed using a free neutron at rest (no Fermi momentum) as a target.

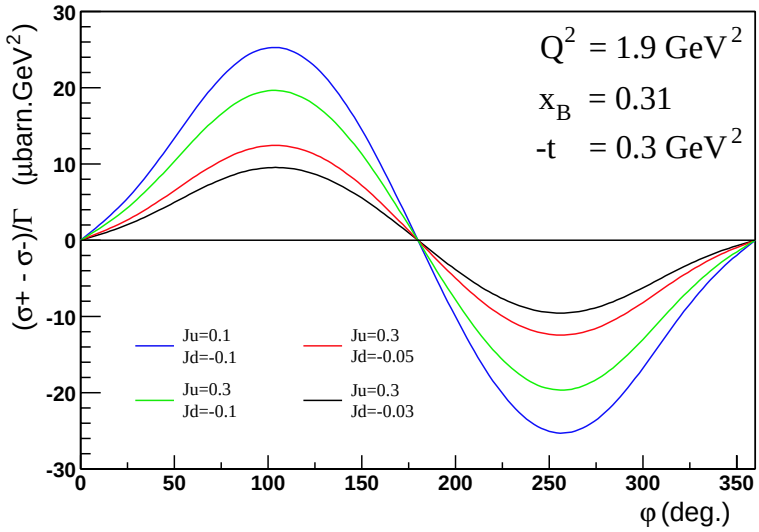

Figure 5: Neutron DVCS cross-section difference divided by $\Gamma(x_B, y, \Delta^2, \phi)$ as defined in this section, evaluated at $Q^2 = 1.9$ GeV^2, $x_B = 0.31$ and $-t = 0.3$ GeV^2 as a function of the azimuthal angle φ for different values of the parameters J_u and J_d within one model. J_u and J_d are the fractions of angular momentum carried by the u and d quarks in the proton which enter in Ji's sum rule. The only constraints to the GPD E comes from these parameters through Ji's sum rule, but they are totally unknown [15]. Note that the curves have been computed using a free neutron at rest (no Fermi momentum) as a target.

The next two sections will give an overview of the existing DVCS setup and the recoil neutron detection strategy.

3.1 The regular DVCS setup

The DVCS setup has been primarily designed for the proton experiment E00-110. The design work is achieved and all detectors will be constructed in the first half of 2003, and tested until the experiment starts (planned in March 2004). The design of the DVCS detectors is shown in Fig. 7 in its almost final state. The platform which will allow this detector to be moved to each new setting will be designed by Jefferson Lab, based on the BigBite stand. High rates are expected in this experiment since bare scintillators are located at small angles relative to the beamline. Since the generated pile-up might be a problem, a novel data acquisition has been developed: the use of ARS (Analog Ring Sampler) which act as 1 GHz Flash-ADCs for all the channels of this experiment will allow us to handle pile-up events in a clean manner.

3.2 Proton Array

In order to detect the recoil protons, we are constructing a 100 element plastic scintillator array. This array is matched to the out-of-plane acceptance required to measure the beam helicity asymmetry in deeply virtual kinematics. The array subtends polar angles 18 to 38 degrees in five rings around the central $\vec{q}$ direction. Each ring is divided into 20 elements that together subtend azimuthal angles from 45 to 315 degrees (the gap is required for the beam and scattered electron). For each $e\gamma$ coincidence, we can predict the direction of the outgoing proton, under the assumption of a $eN \rightarrow eN\gamma$ event.

DVCS events will be separated from background according to the separation between the predicted direction of the nucleon and the direction of the coincident particle (if any) in the proton array. The angular resolution of the proton array is consistent with the convoluted resolutions of the electron spectrometer and photon calorimeter.

The proton array is constructed of EJ-200 scintillator coupled to Photonis XP2972 1 1/8" PMTs. Each PMT will be read out by one ARS channel (see DAQ description in subsection 3.4). Mechanically, the array is constructed of 20 identical towers (Fig. 8), each spanning 13.5° degrees in azimuth and polar angles 18–38°. To handle the large flux of low energy particles (below the 20 MeVee detection threshold), the PMTs are operated at low gain ($\approx 10^4$) and coupled to an active base (gain 40). The base also provides a monitor of the DC anode current via an ADC read by EPICS.

3.3 Calorimeter

The calorimeter for the DVCS experiment will consist of 132 blocks of lead fluoride, each with dimension 30 mm × 30 mm × 184 mm. Lead fluoride is very dense ($\rho = 7.66$ g/cm^3), with a short radiation length ($X_0 = 0.95$ cm) and a small Moliere radius ($r_M = 2.22$ cm), which allows it to be built into a compact calorimeter. Each block will be viewed by a squarish fine-mesh Hamamatsu R5900U PMTs connected to an active base, providing the required gain and a DC anode current monitoring similarly to the proton array. Finally, each PMT will be read out by one ARS channel. A nine-cell prototype calorimeter was constructed and tested in Hall A during the March 2002 test run. The resulting resolution as a function of energy is seen in Fig. 9. The curve shown in the figure is the result of a fit with the function $\sigma/E = a \oplus b/\sqrt{E}$. The fit yields a resolution of $1.6\% \oplus 3.6\%/\sqrt{E}$.

3.4 Data Acquisition

Unlike the dedicated DVCS detectors, the spectrometer's acquisition system consists of conventional ADCs and TDCs. The standard electron arm trigger will provide the first level trigger T1 when a good electron candidate is detected. However, the calorimeter and proton array information are recorded using a novel system: Analog Ring Samplers (ARS). These new devices based on a silicon chip developed by CEA/Saclay have been studied, designed, and produced at the LPC-Clermont. Each

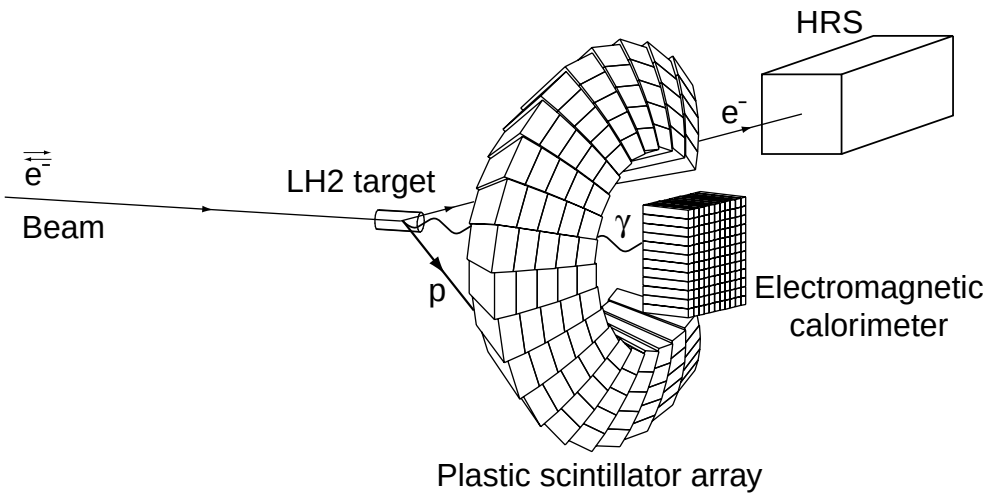

Figure 6: Schematic of the DVCS setup for experiment E00-110. The incoming electron scatters on the 15 cm LH2 target. The scattered electron is detected in the left HRS, the recoil proton is detected in a 100-block scintillator array and the emitted photon is detected in a 132-block lead-fluoride calorimeter.

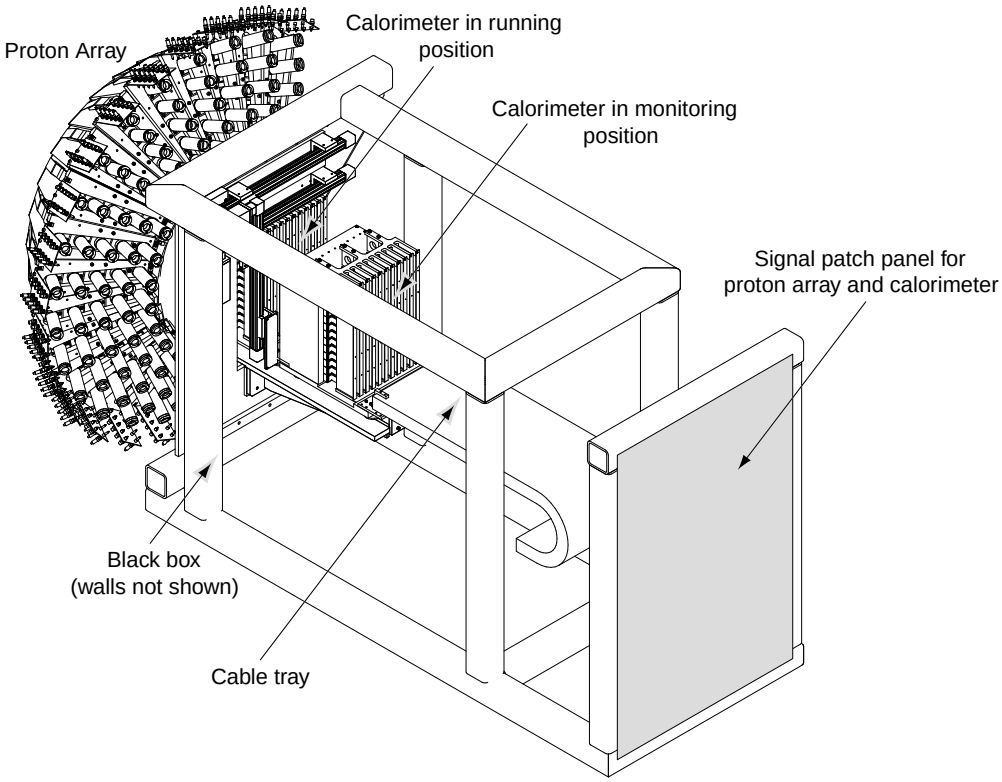

Figure 7: Full view of the DVCS arm in the current state of the design showing the proton array, the calorimeter and the black box protecting the calorimeter from the light (the walls are not shown).

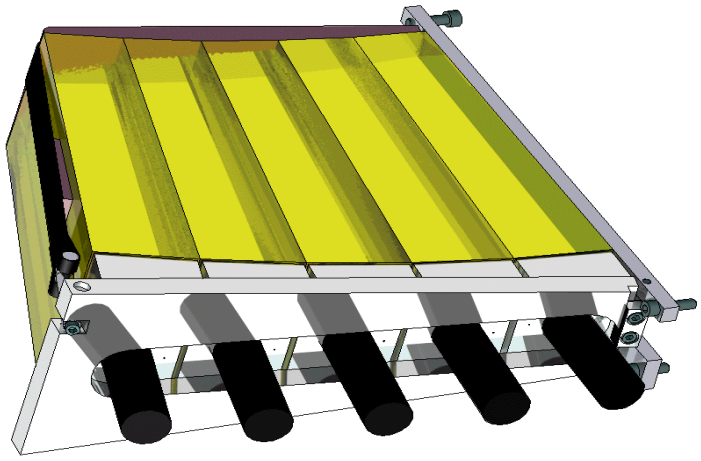

Figure 8: CAD drawing of a 5-element "tower" from the proton array. One such prototype tower was tested successfully in March 2002.

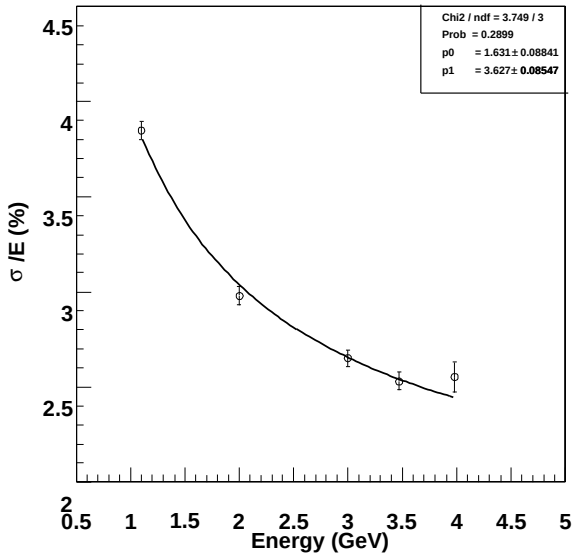

Figure 9: The resolution of the nine-cell PbF_2 test calorimeter as a function of energy. The data has been fit with the function $\sigma/E = 1.6\% \oplus 3.6\%/\sqrt{E}$.

channel of the detectors is continuously sampled and stored on a 128-capacitor ring at a frequency of 1 GHz. The trigger signal T1 stops this process and freezes the information in the capacitors. A second level trigger T2 starts the extraction (1 MHz). Each of the 128 capacitors of the ring is digitized using a 12-bit ADC, yielding a 128 ns long waveform representing the signal during a predefined time window. Offline, this information is processed and used to extract the amplitudes and times of signals like conventional ADCs and TDCs. This is extremely powerful to resolve pile-up events on which a careful waveform analysis can be performed to disentangle the signals arriving close in time, as shown in Fig. 10.

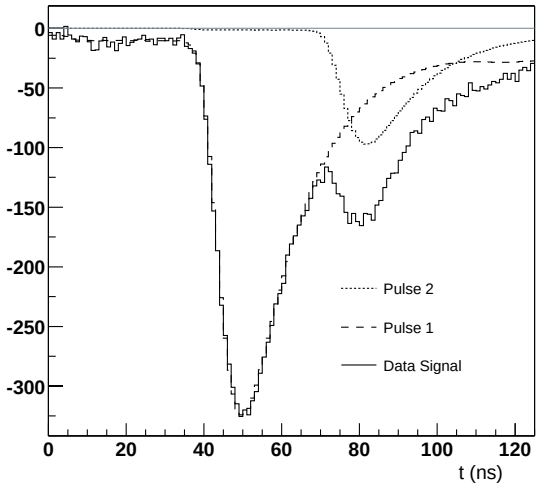

Figure 10: Typical waveform recorded by an ARS channel, yielding two pulses. A waveform analysis is performed to get the information about the two separate pulses.

Using the ARS leads to an increase of the data rate roughly by a factor of 64 compared to conventional electronics. It is therefore necessary to have a selective second level trigger T2. We have built our T2 trigger using parallel digital electronics to find clusters in the PbF_2 calorimeter. The analog signals from all blocks are split, with one branch to the ARS and the second to a 7-bit Flash-ADC (FADC) with a programmable integration time (typically 30 ns). The FADC is triggered by the T1 trigger (electron arm). For all contiguous groups of 2×2 blocks in the calorimeter, a "sum-of-4" is calculated in parallel and compared to a programmable energy threshold. This threshold can be high, since the DVCS photons have at least 1.5 GeV in all kinematics. If at least one 2×2 cluster is above threshold, the second level trigger T2 is generated, initiating the readout of the ARS. If no high energy cluster is found, the ARS is given a fast clear and the data acquisition is re-enabled with a 350 ns total dead-time between T1 and re-enable. For valid events, the T2 electronics also records the values of all 132 FADC channels, and the list of all 2×2 clusters above threshold. This information is therefore available for pre-analysis.

3.5 Neutron detection and identification

Thanks to its large thickness, the proton array is a rather efficient neutron detector. Indeed, calculations performed with the GEANT package and reported in Fig. 11, show that the expected neutron efficiency of a scintillator block is typically 20 % depending on the software threshold and the neutron momentum. However, a single energy deposit in the proton array, even in coincidence with a possible DVCS event defined by the electron spectrometer and the photon calorimeter, does not allow to identify the nature of the particle. Ultimately, one has to discriminate between DVCS protons and neutrons that both originate from the deuterium target. There are two possibilities to overcome this problem:

i) *Shielding:* a 1 to 2 cm plate of iron placed between the target and the proton array has the double advantage of stopping a lot of low momentum protons and of protecting the array against electromagnetic background without having a strong impact on the neutron detection efficiency;

ii) *Additional ΔE detectors:* a 2 to 3 cm thick scintillator paddle placed in front of a scintillator block of the proton array, allows to identify charged particles with a very high efficiency while having a low efficiency to neutral particles; therefore an additional ΔE detector acts as a charged particle tagger.

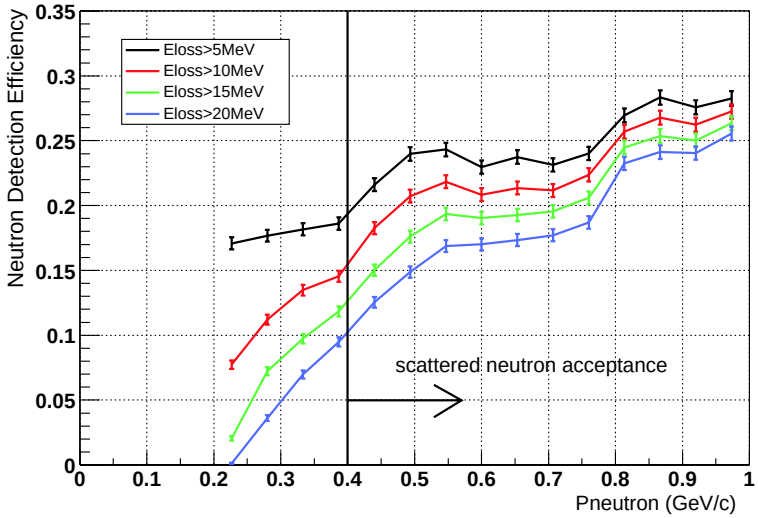

Figure 11: Neutron detection efficiency of the proton array as a function of neutron momentum. The four curves are for different thresholds (respectively 5, 10, 15 and 20 MeV). This is the result of a GEANT simulation taking into account a realistic setup as well as a 2 cm-thick iron shield and a 2 cm-thick layer of tagger paddles. The recoil neutron acceptance of our experiment is from 400 MeV/c to 1000 MeV/c.

The current detector system which is foreseen for this experiment combines these 2 possibilities in a design which is currently being optimized. A scheme of principle of the DVCS tagger is shown in Fig. 12. Two scintillator paddles are placed in front of each tower of the proton array, one paddle overlapping with half of the 5 blocks of a tower. The paddles are disposed along the generatrices of a cone whose center is located on the main axis of the DVCS detector. At the bottom part, the paddles lay on a C-shape aluminum support whose external surface consists of a multifaceted polygon, each of them corresponding to a paddle. This scheme increases advantageously the mechanical rigidity of the whole device. A separate second layer of ΔE scintillators with equivalent geometry is envisioned in order to improve the quality of charged particle tagging and to reduce the efficiency to neutral particles by requiring the absence of a signal in each layer for neutron identification. Not shown on the figure, photo multiplier tubes are placed on the top of the paddles. The output signals will be implemented in the *standard* electronics of the DVCS setup, based on ARS chips. A 2 cm iron plate, placed in front of each couple of paddles, shields simultaneously the ΔEs and the blocks of a tower. Additional mechanical support might be arranged via a fixation to the cart that support the DVCS setup.

The actual design of the DVCS tagger is still under study. Two parameters are being optimized: the thickness of the ΔEs and the material and thickness of the shielding plate. Fig. 13 shows the simulated counting rate in paddle # 3 (one of the paddles close to the beam pipe) for a $4.2{\cdot}10^{37}$ $\mathrm{cm}^{-2}\mathrm{s}^{-1}\mathrm{nucleon}^{-1}$ luminosity as a function of software threshold for different scintillator thicknesses and a 2 cm shielding plate of iron. This threshold can be compared with the minimum

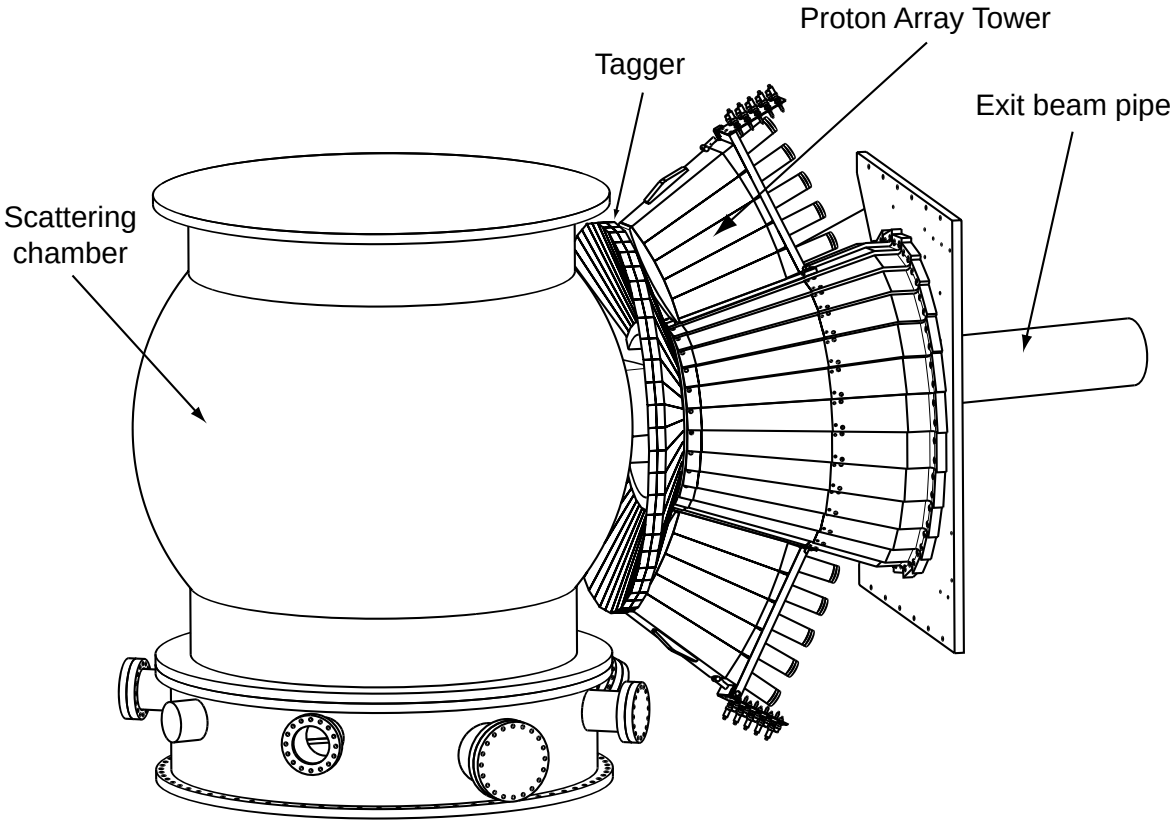

Figure 12: Detector layout with 2 layers of scintillator paddles as a tagger for protons.

energy deposited by DVCS protons (3 MeV/cm at 1 GeV/c). The nominal operational rate of the electronics readout is up to 10 MHz [2]. Applying this limit in Fig. 13 shows that a 2 cm thick scintillator combined with a 5 MeV threshold allows the detection of these DVCS protons. Larger thicknesses are also possible but have larger efficiencies to neutral particles, leading to misidentification of neutrons. However, there are additional effects which may affect the amplitude of the signal, among them: light attenuation in the paddle, light collection, photomultiplier tube efficiency... These result in fluctuations of the signal amplitude which may require smaller thresholds and hence may hit the 10 MHz limit. These effects are currently being studied through dedicated simulations using the LITRANI (LIght TRacking in ANIsotropic media) package; the construction of prototype paddles is also envisaged.

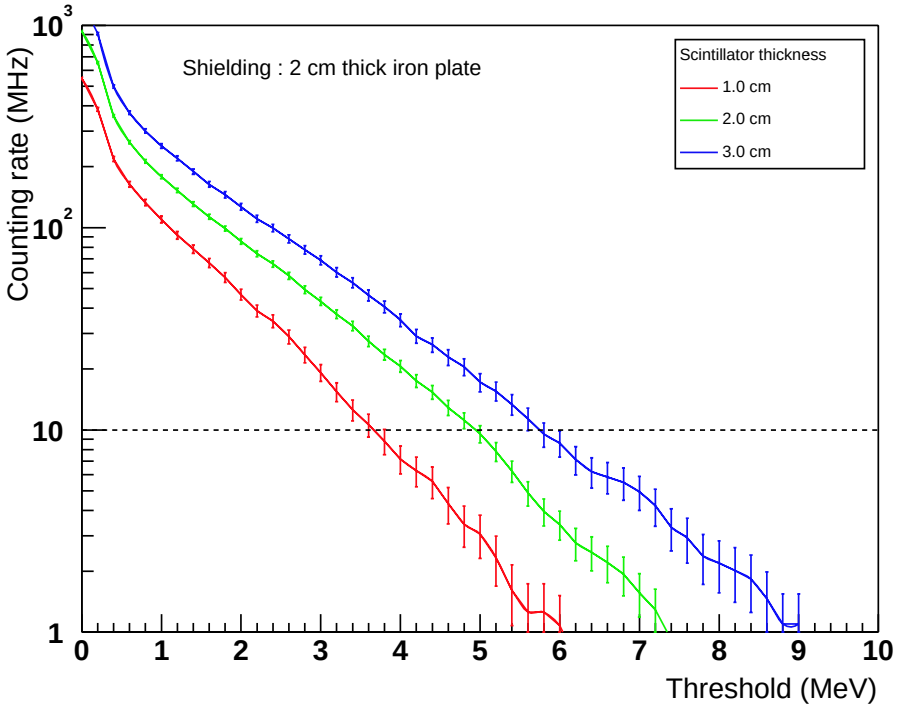

Figure 13: Simulated counting rate in paddle #3 (one of the paddles closest to the beam pipe) for a $4.2{\cdot}10^{37}$ $cm^{-2}s^{-1}nucleon^{-1}$ luminosity as a function of a software threshold for different scintillator thicknesses and a 2 cm shielding plate of iron.

Fig. 14 shows the counting rate for a 2 cm-thick ΔE and a $4.2{\cdot}10^{37}$ $cm^{-2}s^{-1}nucleon^{-1}$ luminosity as a function of the threshold for several thicknesses of the iron shielding plate. It is clear from this figure that the 1 cm plate fulfils the requirements of the electronics readout. A more detailed study of the electromagnetic background is underway in order to investigate the use of lighter materials.

Finally, Fig. 15 shows the integrated counting rate in the first ΔE layer for the 1×2 (shielding thickness, scintillator thickness) setup and a typical 4 MeV threshold: the whole system is operational if one cuts the 3 lowest angle paddles as shown. These results are in agreement with the measurements of the DVCS test run on a liquid hydrogen target which showed that the blocks within the angular range 16°-26° might have to be shutdown or have extra shielding because of high counting rates. These results also seem to indicate that the unitary segmentation - 2 paddles per tower - might not be required for most of the towers. In any case, further studies are under way to fine tune the tagger system but we are confident that such a detector will achieve very good proton/neutron discrimination over more than 95% of the scintillator array acceptance at the designed luminosity.

[2] one additional pulse in a 100 ns time window, which can be discriminated by performing a waveform analysis

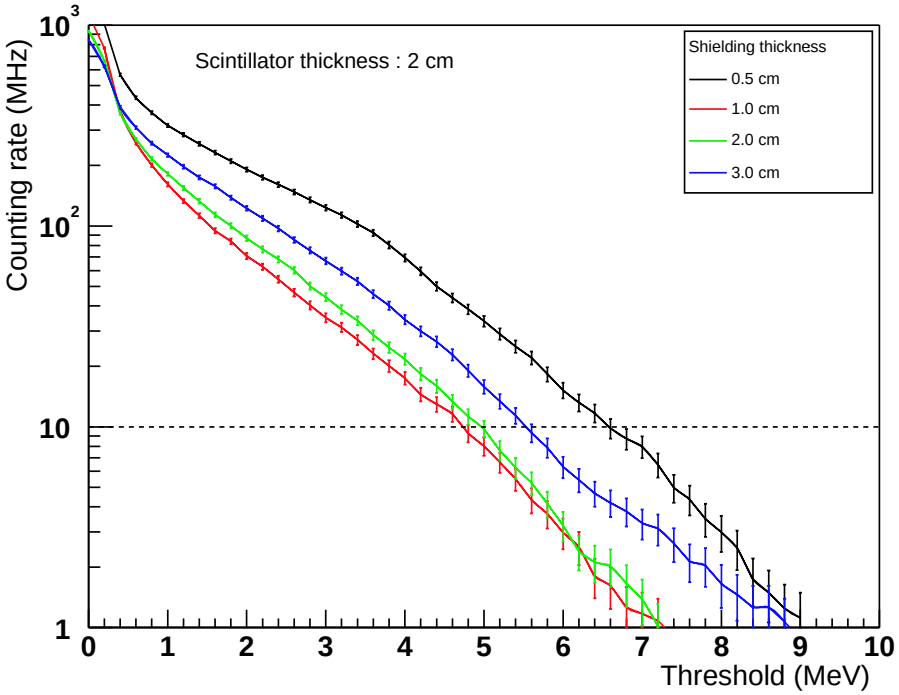

Figure 14: Simulated counting rate in paddle #3 for a 2 cm-thick ΔE and a $4.2{\cdot}10^{37}$ $\mathrm{cm}^{-2}\mathrm{s}^{-1}\mathrm{nucleon}^{-1}$ luminosity as a function of the threshold for several thicknesses of the iron shielding plate.

Note that the electromagnetic background simulation has been successfully double-checked with test run data. This was a requirement of the readiness review for the E00-110 experiment. It is therefore a rather good estimate to fine tune our experimental setup and check if the detectors can be used at the designed luminosity for the neutron DVCS experiment.

3.6 Fermi motion effects

Using deuterium as a quasi-free neutron target means that the kinematics of the DVCS reaction is blurred by the Fermi motion of the nucleon inside the deuteron. However, the deuteron is a weakly bound nucleus and the recoil momentum of nucleons in the DVCS reaction is much higher (from 400 MeV/c up to 1000 MeV/c) than the Fermi momentum of nucleons inside the deuteron (typically of the order a few tens of MeV, see Fig. 16 and Fig. 17). This actually justifies using the **impulse approximation** for the treatment of the neutron inside the deuteron. Note that the impulse approximation is used all along this proposal and especially for the estimation of counting rates and expected results towards the end of this section.

As shown on the top part of Fig. 18, the Fermi motion complicates the DVCS diagram further: In addition to the usual angles θ_{DVCS} and φ_{DVCS}[3], one can define additional polar and azimuthal angles θ_{fermi} and φ_{fermi} which characterize the effect of the Fermi momentum of the target nucleon. The DVCS kinematics implies that the Fermi motion cone (defined by θ_{fermi} and φ_{fermi}) is much "smaller" than the DVCS cone (defined by θ_{DVCS} and φ_{DVCS}) as shown on the bottom plot of Fig. 18.

The effect of Fermi motion depends on which observable one wants to access. In the impulse approximation, the single spin asymmetry is completely insensitive to Fermi motion effects except for the smearing of some kinematical variables. Table 3 gives a comparison of the expression of the main

[3]defined as the angle between the leptonic and photonic planes which does not depend on whether the target nucleon is at rest or not

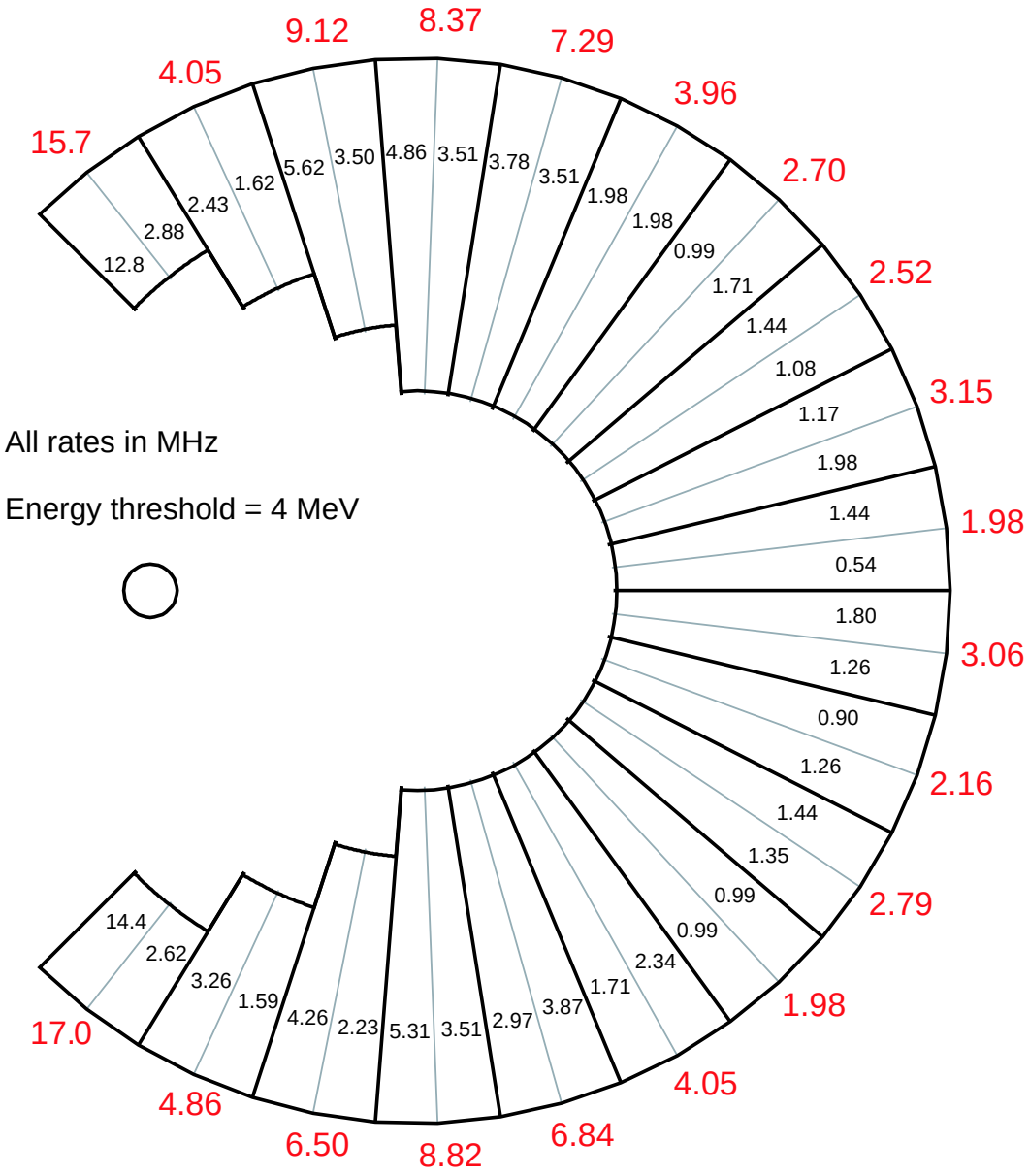

Figure 15: Simulated counting rates for a 2 cm-thick ΔE, a 1 cm-thick iron shield and a typical 4 MeV threshold at a $4.2{\cdot}10^{37}$ $cm^{-2}s^{-1}nucleon^{-1}$ luminosity. The rate written in black in each sector represents the rate in MHz for that sector, the rate written in red outside the sector represents the sum of the rates in the two corresponding sectors. Low angle paddles have been cut out to maximize the acceptance and to keep manageable counting rates.

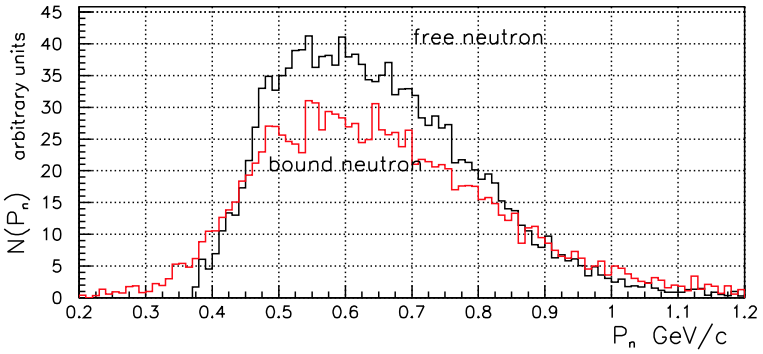

Figure 16: Momentum distribution of the recoil neutrons accepted in E00-110 detectors for free neutrons and bound neutrons.

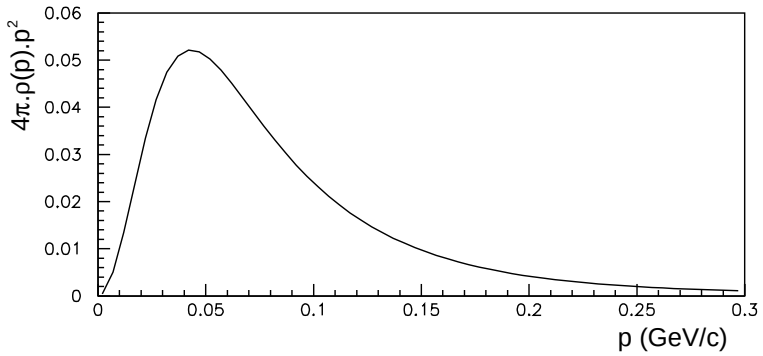

Figure 17: Momentum distribution of nucleons inside the deuteron $p^2\rho(p)$, including the phase-space factor (from [16])

kinematical variable we use for the analysis in the case of an initial nucleon at rest and a nucleon inside the deuteron:

Note that the ratio p_f/M is of the order 1/10 and since the orientation of $\vec{p_f}$ is isotropic, there is no effect on the average of all Fermi-motion dependent variables assuming it is integrated over all φ_{fermi}. Moreover, all acceptance effects cancel out in the relative asymmetry. Note that even though the main goal of the experiment is to measure the absolute DVCS cross-section difference, the relative asymmetry can easily be compared to models and as such, will be extracted in the first stage of the analysis.

In addition, it is interesting to note that the missing mass width is almost not affected by the Fermi motion effect. The correction factor $2\vec{p_f} \cdot \vec{p'} \approx 0.03$ GeV^2 does not contribute at all compared to experimental resolutions. The exclusivity of our experiment in terms of a cut on the missing mass will be exactly the same as in the free proton experiment.

3.7 Competing channels

Just as in the proton experiment, there are two competing channels to the DVCS process:

- the π^0 electroproduction (Fig. 19),
- the pion associated production (Fig. 20), or associated DVCS (ADVCS).

In order to select DVCS events one must make sure that we select photon electroproduction events. Two techniques are used:

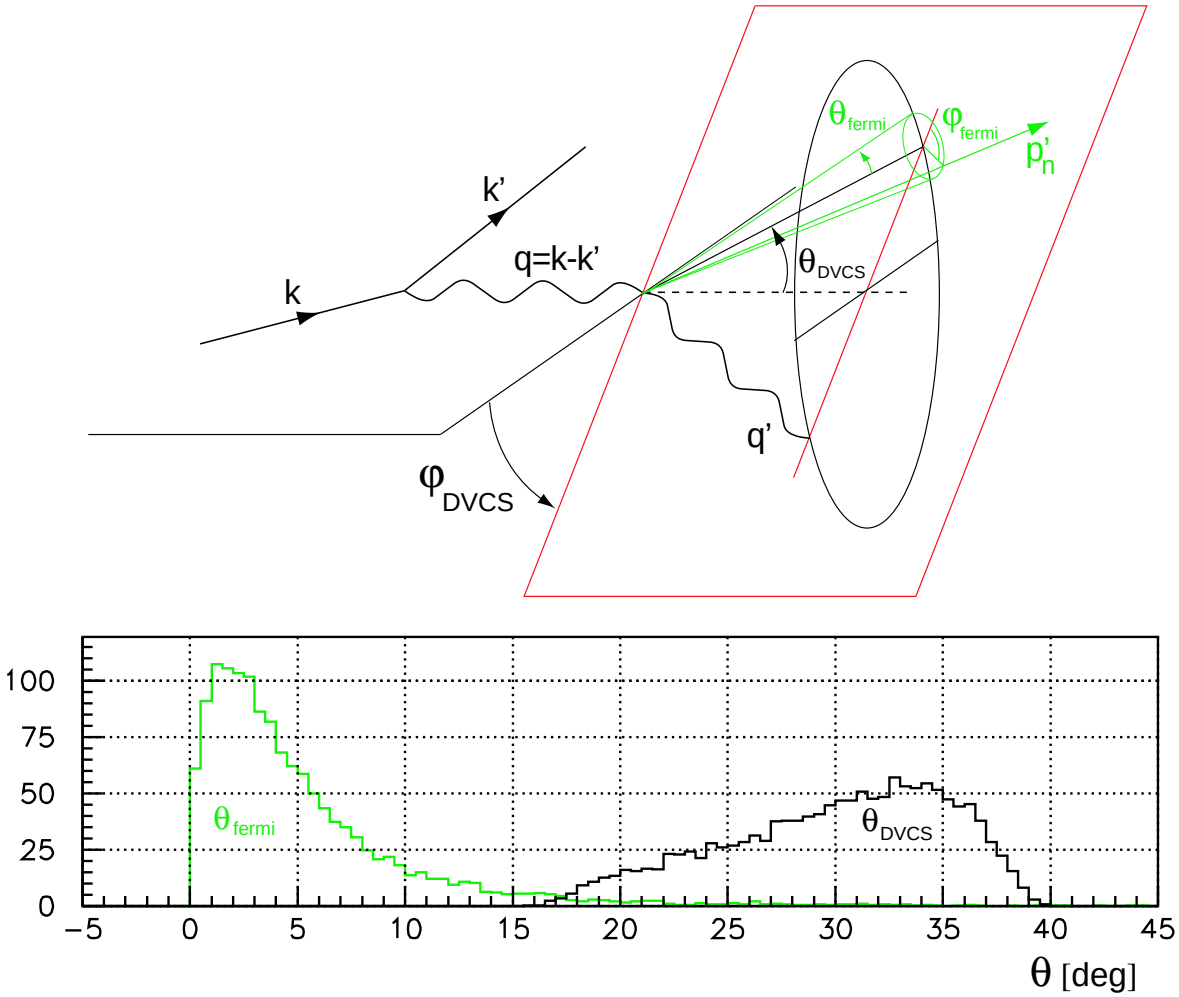

Figure 18: Top figure: Sketch of the DVCS reaction when the initial nucleon has some Fermi momentum. In addition to the usual angles $\theta_{\rm DVCS}$ and $\varphi_{\rm DVCS}$, one can define additional polar and azimuthal angles $\theta_{\rm fermi}$ and $\varphi_{\rm fermi}$ which characterize the effect of the Fermi momentum of the target nucleon. Bottom figure: polar angles of the DVCS ($\theta_{\rm DVCS}$)and Fermi ($\theta_{\rm fermi}$)cones as defined earlier.

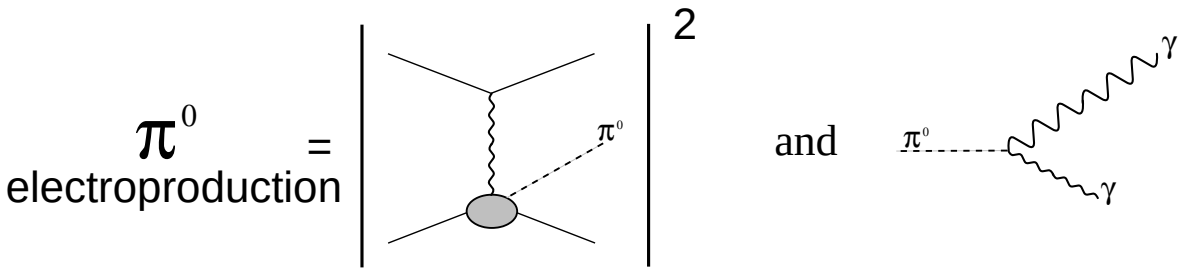

Figure 19: π^0 electroproduction diagram. This process can mimic DVCS when there is a very forward high energy photon and a small backward photon which remains undetected. The missing mass technique cannot discriminate between DVCS and this process. The solution is to select symmetric π^0 decay events for which both photons are detected in the calorimeter. Using this technique, one can extrapolate the π^0 background and subtract its contribution from the DVCS events.

Free nucleon at rest	Nucleon in the impulse approximation $\left(\frac{p_f}{M} \sim \frac{1}{10}\right)$
$\mathbf{p}(M,0)$	$\mathbf{p}(\sqrt{M^2+\vec{p_f}^{\,2}},\vec{p_f}) \simeq \mathbf{p}(M[1+\Theta(\frac{\vec{p_f}^{\,2}}{M^2})],\vec{p_f})$
$Q^2 = (\mathbf{k}-\mathbf{k'})^2$	$Q^2 = (\mathbf{k}-\mathbf{k'})^2$
$\Delta = (\mathbf{k}-\mathbf{k'}-\mathbf{q'})$	$\Delta = (\mathbf{k}-\mathbf{k'}-\mathbf{q'})$
$x_B = \frac{Q^2}{\mathbf{p}\cdot(\mathbf{k}-\mathbf{k'})} = \frac{Q^2}{2M\cdot(k-k')}$	$x_B \simeq \frac{Q^2}{2M\cdot(k-k')}[1+\frac{\vec{p_f}\cdot(\vec{k}-\vec{k'})}{M\cdot\lvert(\vec{k}-\vec{k'})\rvert}+\Theta(\frac{\vec{p_f}^{\,2}}{M^2})]$
$y = \frac{\mathbf{p}\cdot(\mathbf{k}-\mathbf{k'})}{\mathbf{p}\cdot\mathbf{k}} = \frac{k-k'}{k}$	$y \simeq \frac{k-k'}{k}[1+\frac{\vec{p_f}\cdot(\vec{k}-\vec{k'})}{M\lvert\vec{k}-\vec{k'}\rvert}-\frac{\vec{p_f}\cdot\vec{k}}{M\lvert\vec{k}\rvert}+\Theta(\frac{\vec{p_f}^{\,2}}{M^2})]$
$Q^2\mathcal{P}_1 = (\mathbf{k}-\mathbf{q'})^2 \qquad Q^2\mathcal{P}_2 = (\mathbf{k}-\mathbf{\Delta})^2$	$Q^2\mathcal{P}_1 = (\mathbf{k}-\mathbf{q'})^2 \qquad Q^2\mathcal{P}_2 = (\mathbf{k}-\mathbf{\Delta})^2$
$\phi = Angle(\vec{k}\times\vec{k'};(\vec{k}-\vec{k'})\times\vec{q'})$	$\phi = Angle(\vec{k}\times\vec{k'};(\vec{k}-\vec{k'})\times\vec{q'})$
$p' = \mid \vec{k}-\vec{k'}-\vec{q'} \mid$	$p' = \mid \vec{k}-\vec{k'}-q' \mid [1+\frac{\vec{\lvert\vec{p_f}\rvert}}{\lvert\vec{k}-\vec{k'}-\vec{q'}\rvert}]$
$\phi_p = \pi - \phi$	$\phi_p = \pi - \phi + \frac{\lvert\vec{p_f}\sin\phi'\rvert}{\lvert\vec{k}-\vec{k'}-\vec{q'}\rvert}[1-\frac{\vec{p_f}\cdot(\vec{k}-\vec{k'})}{\lvert\vec{p_f}\rvert\lvert\vec{k}-\vec{k'}\rvert}]+\Theta(\frac{\vec{p_f}^{\,2}}{M^2})$
$M_X^2 = (\mathbf{k}+\mathbf{p}-\mathbf{k'}-\mathbf{q'})^{\mathbf{2}} = M^2$	$M_X^2 = M^2 - 2\vec{p_f}\cdot\vec{p'}$
$\epsilon = 2x_B\frac{M}{Q} \qquad \xi = x_B\frac{1+\frac{\Delta^2}{2Q^2}}{2-x_B+x_B\frac{\Delta^2}{Q}}$	$\epsilon = 2x_B\frac{M}{Q} \qquad \xi = x_B\frac{1+\frac{\Delta^2}{2Q^2}}{2-x_B+x_B\frac{\Delta^2}{Q}}$

Table 3: Comparison of the expression of the main kinematical variable in the case of an initial free nucleon at rest and a nucleon inside the deuteron (treated in the impulse approximation).

- a missing mass cut in $e'\gamma X$,
- check that the measured direction of the detected neutron coincides (within resolution and Fermi motion smearing) with the expected direction inferred from the measurements of the scattered electron and emitted photon and the assumption of DVCS kinematics.

As explained in the previous section, the missing mass technique is as powerful for this experiment as for the free proton experiment, since Fermi motion has almost no effect on the width of the missing mass. Figure 21 shows the expected resolutions and distributions for DVCS events, π^0 electroproduction and ADVCS. A missing mass cut $\left|M_X^2 - M_n^2\right| < 0.5$ keeps most DVCS events and the parasitic reaction contamination is kept under 3%.

The comparison of the direction of the recoil particle is much more sensitive to Fermi motion effects than the missing mass technique. As shown on Fig 18, $\varphi_{fermi} \sim 5^\circ$. Therefore, our position resolution on the scintillator array is the convoluted resolution of the HRS and calorimeter with this Fermi motion smearing: instead of checking for a neutron in ∼1 scintillator array block (which size corresponded to our resolution without Fermi motion effects), we will now look into a cluster of 6 to 9 scintillator blocks. The added exclusivity check is not as powerful as in the no-Fermi-motion case, but will still help removing more than half of the remaining contamination by parasitic reactions. We expect that the remaining contamination will be no larger than 1-2% of our DVCS sample. In any case, it is important to note that the parasitic reactions will be studied and their effect on the DVCS cross-sections and asymmetry will be subtracted.

3.8 Final state interactions

Final state interactions can give rise to false asymmetries proportional to the total neutron nucleon cross-section. This effect is expected to be very small, of the order of 1% to 3% according to qualitative estimates from theorists [17]. The quantitative evaluation is under way and will be used for the physics analysis. In any case, if the acceptance of the recoil nucleon was 4π or if we did not try to detect the recoil nucleon, all the effects would cancel out (these rescattering effects once integrated over the induced phase vanish). In the middle of our scintillator array, there won't be any effect since it will be integrated over. The asymmetry will only be non-zero at the edge of our acceptance where we cannot integrate over the induced phase. We expect that only ∼20% of our acceptance will be affected and will have a false asymmetry, which is once again expected to be small. If the effect is larger than expected, a model will be included into the Monte-Carlo simulation and taken into account.

3.9 Physics analysis

The goal of the experiment is to extract the values of the A and B coefficients corresponding to the twist-2 and higher-twist contributions which appear in the difference of cross-sections for opposite helicities:

$$\frac{d\overrightarrow{\sigma}}{dx_B dy dt d\varphi} - \frac{d\overleftarrow{\sigma}}{dx_B dy dt d\varphi} = \Gamma(x_B, y, t, \varphi) \cdot (A \sin\varphi + B \sin 2\varphi)\,.$$

The $\sin\varphi$ coefficient has no Q^2 dependence and can be written as:

$$A = F_1(t)\mathcal{H} + \frac{x_B}{2 - x_B} \cdot (F_1(t) + F_2(t)) \cdot \widetilde{\mathcal{H}} - \frac{t}{4M^2} F_2(t)\mathcal{E}\,.$$

The $\sin 2\varphi$ coefficient B is expected to have a $1/Q$ dependence. We will extract the A coefficient using the following method. The difference between the number of counts (binned in φ and t) for opposite helicities can be written as [4] :

[4] Taking into account the experimental integration over Fermi momentum.

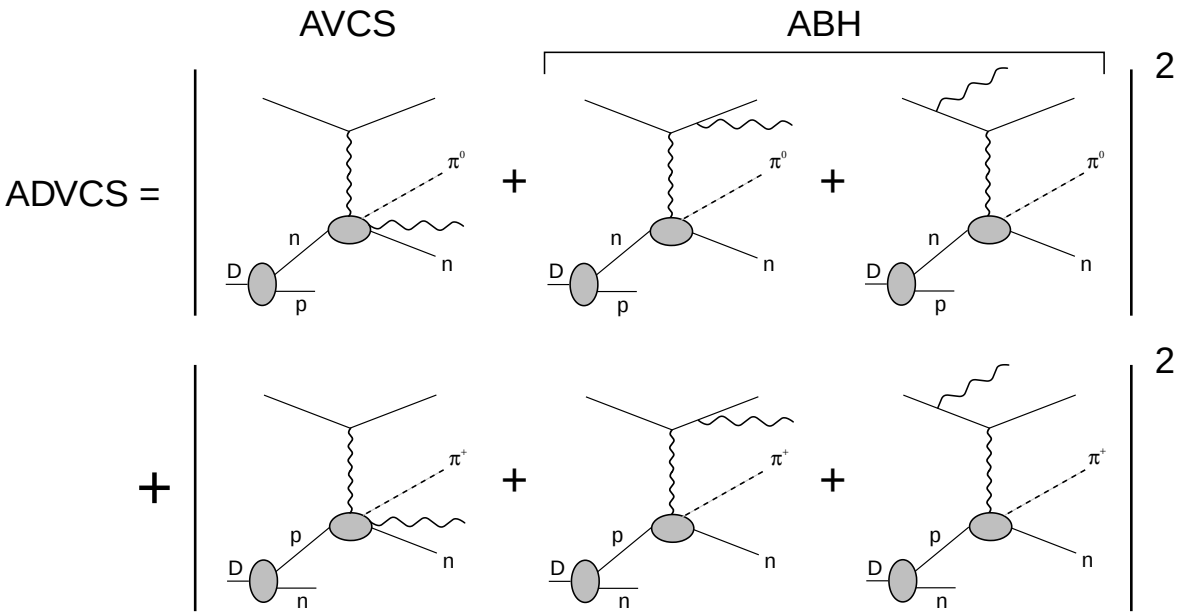

Figure 20: Associated DVCS channels where one extra pion is emitted. All diagrams resulting in a fast recoil proton instead of a neutron have been removed since they will be veto-ed with our tagger system. One can use both the missing mass and recoil particle direction check techniques to limit the number of ADVCS events in the DVCS event sample. However, just like in the π^0 case, ADVCS reactions can be studied and their contribution can be subtracted and corrected.

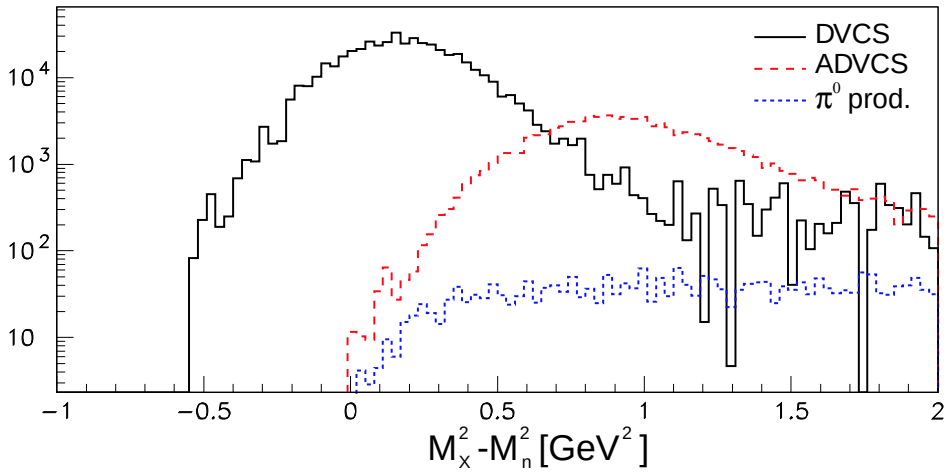

Figure 21: Missing particle mass squared minus the neutron mass squared for DVCS events, π^0 electroproduction events and ADVCS events. A missing mass cut $\left|M_X^2 - M_n^2\right| < 0.5$ keeps 97% DVCS events and the parasitic reaction contamination is kept under 3%.

$$\overrightarrow{N}(\Delta\varphi_i,\Delta t_j) - \overleftarrow{N}(\Delta\varphi_i,\Delta t_j) = Lu \int_{\Delta\varphi_i,\Delta t_j} \left(\frac{d\overrightarrow{\sigma}}{dx_B\,dy\,dt\,d\varphi(\rho(p_f)p_f^2 d\vec{p_f})} - \frac{d\overleftarrow{\sigma}}{dx_B\,dy\,dt\,d\varphi(\rho(p_f)p_f^2 d\vec{p_f})}\right) \cdot \mathcal{E}_{ff}(x_B,y,t,\varphi)dx_B\,dy\,dt\,d\varphi(\rho(p_f)p_f^2 d\vec{p_f}) \quad (21)$$

$$= Lu \cdot A(\bar{x}_B,\bar{t_j}) \int_{\Delta\varphi_i,\Delta t_j} \sin\varphi \cdot \Gamma(x_B,y,t,\varphi) \cdot \mathcal{E}_{ff}(x_B,y,t,\varphi)dx_B\,dy\,dt\,d\varphi(\rho(p_f)p_f^2 d\vec{p_f})$$

$$+Lu \cdot B(\bar{x}_B,\bar{t_j},\bar{Q^2}) \int_{\Delta\varphi_i,\Delta t_j} \sin 2\varphi \cdot \Gamma(x_B,y,t,\varphi) \cdot \mathcal{E}_{ff}(x_B,y,t,\varphi)dx_B\,dy\,dt\,d\varphi$$

which we can write in a more simple fashion:

$$\overrightarrow{N}(\Delta\varphi_i,\Delta t_j) - \overleftarrow{N}(\Delta\varphi_i,\Delta t_j) = Lu \cdot A(\bar{x}_B,\bar{t}) \cdot \mathcal{I}1(\Delta\varphi_i,\Delta t_j) + Lu \cdot B(\bar{x}_B,\bar{t},\bar{Q^2}) \cdot \mathcal{I}2(\Delta\varphi_i,\Delta t_j)\ , \quad (22)$$

where:

- the integrals $\mathcal{I}1(\Delta\varphi_i,\Delta t_j)$ and $\mathcal{I}2(\Delta\varphi_i,\Delta t_j)$ are computed using our Monte-Carlo simulation,
- $N(\Delta\varphi_i,\Delta t_j)$ are the collected counts in the bin (i,j) respectively in φ and t,
- $\mathcal{E}_{ff}(x_B,y,t,\varphi)$ represents the efficiency of our detectors.

For each bin in the variable t, we have a system of linear equations (one for each phi bin) from which the A and B coefficients can be extracted. One can make a few remarks about this analysis:

- We never need to know the value of the variable φ in a bin but only if it is within the bin range, therefore most of the experimental resolution on φ vanishes,
- this method does not take in account the radiative corrections, they are expected to be independent of φ at least for the radiation of real photons. In this case they will appear like a global correction factor just like a normalization,
- the results will be given at an average value of the kinematical variables, calculated using the Monte-Carlo simulation.

3.10 Kinematics and expected results

For this proposal, we plan to measure the DVCS single spin asymmetry and helicity dependent cross-section on the neutron for two kinematics using a ∼6 GeV beam [5], at fixed $Q^2 = 1.9$ GeV^2 and for $x_B = 0.31$ and 0.36. Table 4 summarizes the kinematics. Our choice was governed by a number of considerations:

- Measurement at high enough Q^2 to be in the scaling region,
- keep x_B around 0.3-0.4 (in a region where quark GPDs should dominate),
- have a common kinematical point with the proton experiment so that a direct comparison can be achieved,
- obey certain experimental constraints such as detector position and background considerations.

The expected results for the single spin asymmetry and the cross-section difference are shown in Fig. 22 and Fig. 23 for both bins in x_B. For this evaluation, we have used the model in Ref. [15]

[5] 6 GeV is not currently available at Jefferson Lab. However this experiment can run with 5.75 GeV beam and all calculations and expected results have been calculated using the *available* beam energy of 5.75 GeV. The kinematics are only slightly changed if 6 GeV beam is available at the time of the experiment.

s GeV^2	Q^2 GeV^2	x_B	$-t$ range GeV^2	θ_e deg	P_e GeV/c	θ_{γ^*} deg
5.0	1.9	0.31	0.1-0.7	20.80	2.54	-14.92
4.2	1.9	0.36	0.1-0.7	19.32	2.95	-18.25

Table 4: Proposed kinematics for this experiment. θ_{γ^*} is the angle between the virtual photon and the beam, θ_e and P_e are the scattered electron angle and momentum. The average t for both kinematics is close to -0.3.

and the impulse approximation. The results are presented averaged over all values of t within the acceptance. Note that the t acceptance of the experiment is rather generous and data can be binned in t if the asymmetry size permits. This is especially important since x_B and t dependence are the cornerstone of a "femto-photography" study of the nucleon using DVCS [7]. **Let us emphasize that the GPD E which dominates the neutron DVCS beam-helicity dependent cross-sections and asymmetry is almost completely unknown and unconstrained. Therefore, estimations given in this section can be wrong by rather large factors.**

A very interesting side-product of this experiment is a measurement of the same quantities for the proton, but with a somewhat reduced acceptance in t (due to the added shielding which stops part of the low-momenta protons). Since one of the kinematical setting is common with the (free) proton experiment, we will be able to check the size of the nuclear effects on the proton and ensure that we understand them.

3.11 Systematic error estimates

The basic systematic error sources associated with the measurement of the difference of cross-section are exactly the same as in the proton case. In addition, one will have contributions coming from the acceptance calculation, neutron efficiency and model dependence of nuclear effects, which one could label "Monte-Carlo" errors. Table 5 gives the source and the corresponding relative systematic error estimates. The relative statistical error for the neutron measurement is on the order 20% or more depending on the size of the measured asymmetry which is impossible to know at this moment. In any case, we believe that the total relative systematic uncertainty can reasonably be kept under 10% as shown on the table, which is still at least a factor two smaller than the relative statistical error.

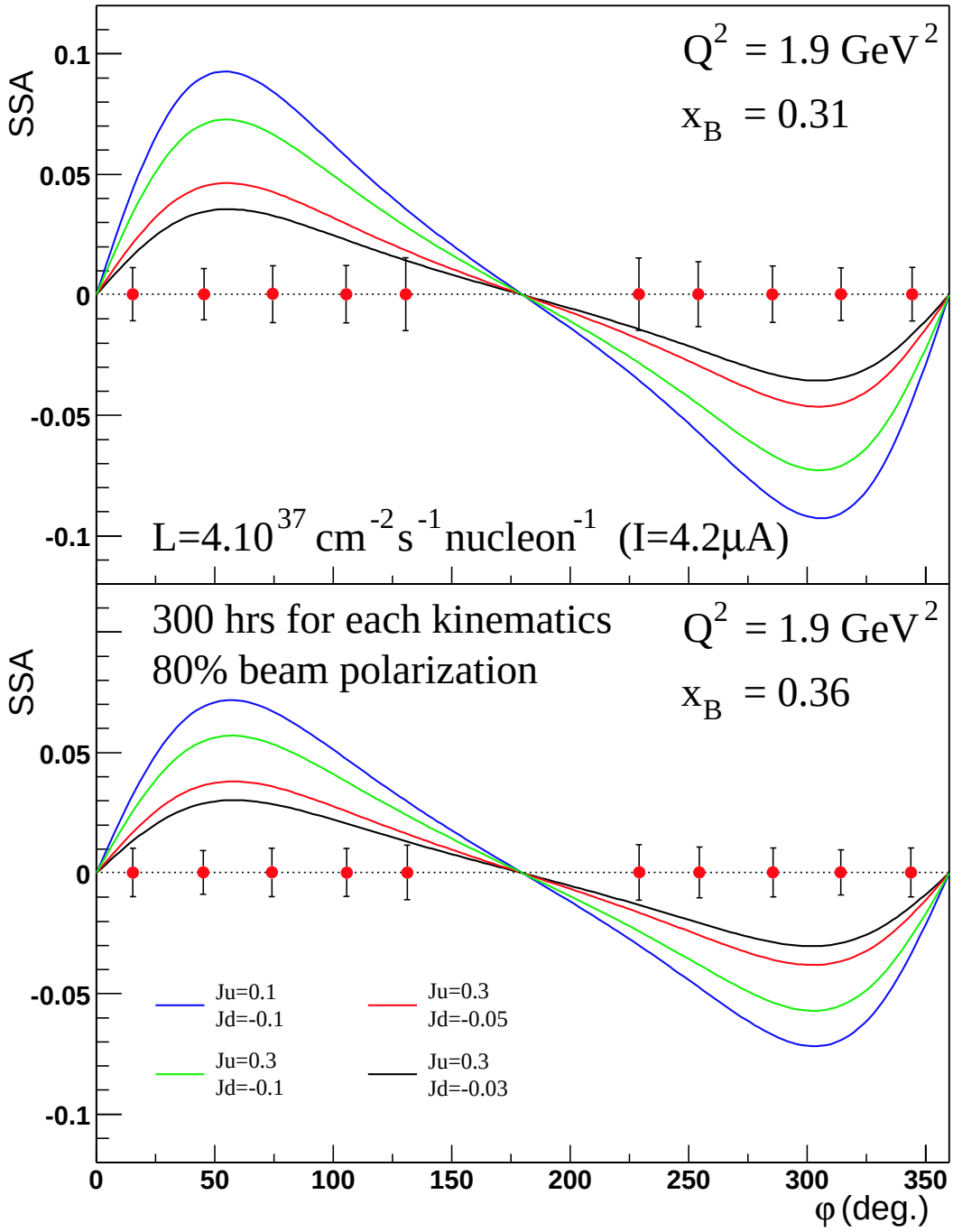

Figure 22: Expected results for the single spin asymmetry in 300 hours of beam time for each kinematical setting at $4{\cdot}10^{37}$ cm^{-2}s^{-1}nucleon^{-1}, corresponding to 4.2μA of beam on the LD_2 target. The curves are predictions from a model for different values of J_u and J_d (see section 2.4 for details). For this evaluation, we have used the model in Ref. [15] and the impulse approximation. Error bars are statistical only.

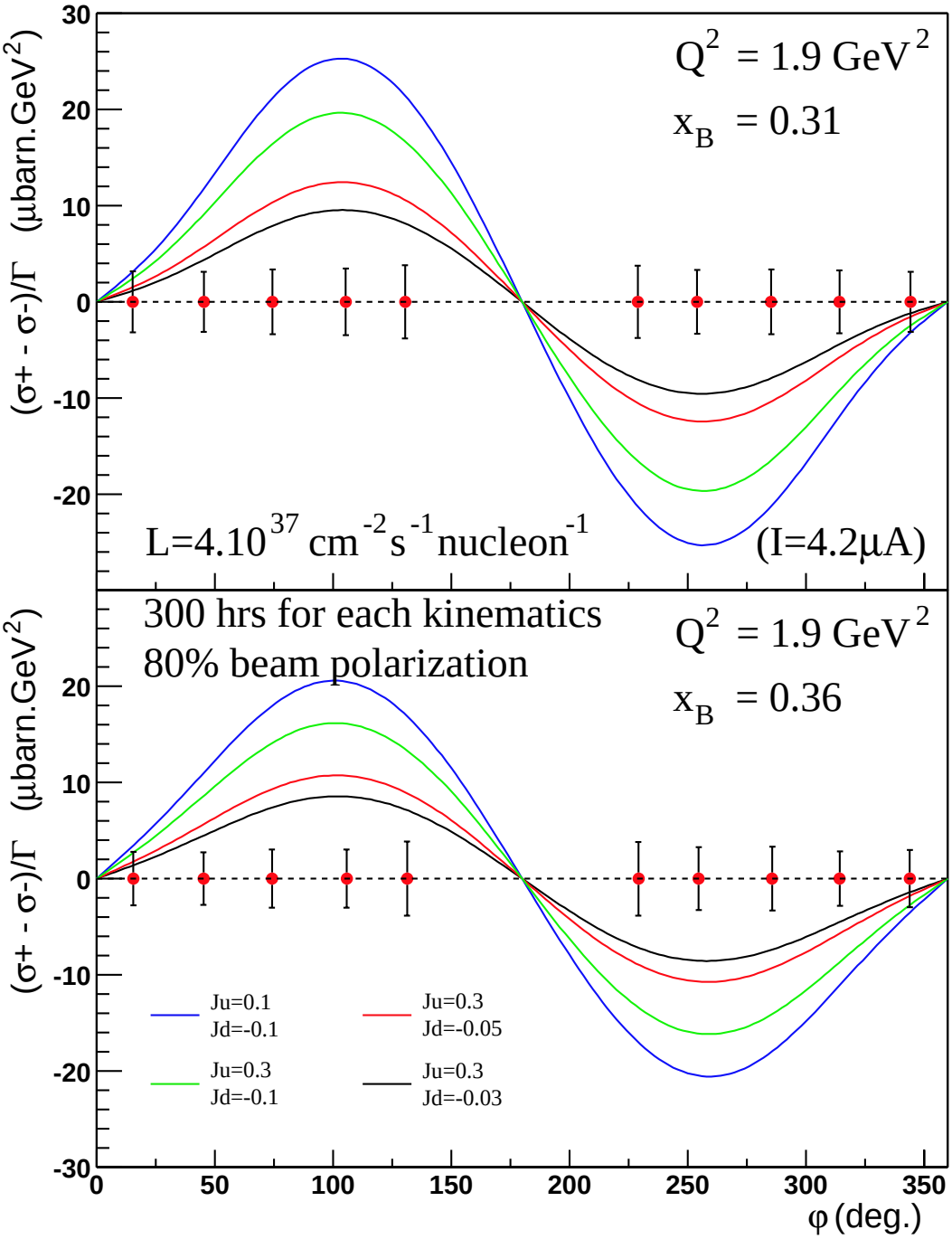

Figure 23: Expected results for the weighted cross-section difference in 300 hours of beam time for each kinematical setting at $4{\cdot}10^{37}$ cm^{-2}s^{-1}nucleon^{-1}, corresponding to 4.2μA of beam on the LD_2 target. The curves are predictions from a model for different values of J_u and J_d (see section 2.4 for details). For this evaluation, we have used the model in Ref. [15] and the impulse approximation. Error bars are statistical only.

		$\overrightarrow{\sigma} + \overleftarrow{\sigma}$	$\overrightarrow{\sigma} - \overleftarrow{\sigma}$	SSA	B/A
Luminosity		1%	1%	-	-
Detection					
	HRS	1%	1%	-	-
	Calorimeter	2%	2%	-	-
	neutron detection	5%	5%	-	-
	proton rejection	1%	1%	-	-
	electronic & acquisition	1%	1%	-	-
	polarisation	-	3%	3%	-
Extraction method (Monte-Carlo)					
	Model	2%	1%	2%	2%
Impulse approximation		1%	1%	1%	-
Exclusivity (contamination)		1-2%	1-2%	1-2%	-
TOTAL experimental (quadratic sum)		6.5%	6.9%	4.2%	2%

Table 5: Relative systematic errors in % on the sum and the difference of cross-sections for opposite helicities and the single spin asymmetry due to the apparatus and the extraction method. The last column gives the systematic errors on the measurement of the ratio of the $\sin\varphi$ to $\sin 2\varphi$ coefficients in the cross-section difference. All values must be understood as conservative estimates.

4 Summary and beam request

The Generalized Parton Distribution (GPD) universe has just been tackled by recent measurements which have confirmed that Deeply Virtual Compton Scattering (DVCS) experiments can be achieved at existing facilities and especially Jefferson Lab at moderate Q^2. Two dedicated experiments in Hall A and Hall B will extract the helicity dependent DVCS cross-sections and asymmetries on the proton in the Q^2 range 1.5-3.5 GeV^2. However, proton experiments can only constrain or extract the H and $\widetilde{H}$ GPDs because of the specific weighting in the asymmetry observable. A neutron DVCS experiment will be mostly sensitive to the least known of GPDs: E. It is essential to access the E GPD not only because it is one of the ingredients in our understanding of the nucleon structure, but also because it enters on equal footings with H in Ji's sum rule, relating H and E to the total angular momentum carried by quarks in the nucleon. Moreover, current GPD models constrain E by a parametrization using fractions of angular momentum carried by the u and d quarks in the nucleon. A comparison of the neutron DVCS single spin asymmetry with these models will yield interesting insights on the nucleon orbital momentum even though Ji's sum rule cannot be accessed with current facilities. Finally, DVCS on the neutron is a unique experiment worldwide: the Hall A setup is very well adapted with its high neutron detection efficiency and large neutron detection solid angle.

We are confident that the experiment can be performed using the regular DVCS equipment in Hall A with an additional charged particle tagger to achieve a good proton/neutron discrimination. The background rates in our detectors have been checked by Monte-Carlo and are manageable. Note that the Monte-Carlo itself has been checked against real test run data and we are confident that it can be used to give a good estimates of background rates in our detectors.

We propose to measure the DVCS beam-helicity dependent cross-sections and asymmetry on the neutron, at fixed $Q^2 = 1.9$ GeV^2 for two values of $x_B = 0.31$ and 0.36. We will use the polarized beam on the 15 cm liquid deuterium target and will detect the scattered electron in the left HRS, the emitted photon in a PbF_2 calorimeter and the

recoil neutron in a scintillator array. In addition to the Hall A DVCS equipment in construction for the proton experiment E00-110, we will add shielding and a charged particle tagger (ΔE veto) in front of the scintillator array. With this modification, we will be able to measure $D(e,e'n\gamma)p$ events, and veto the $D(e,e'p\gamma)n$ events which penetrate the shielding. Each kinematical setting will require 300 hours of 6 GeV, 4.2μA beam at 80% polarization.

References

[1] R. Hofstadter, *Ann. Rev. Nucl. Sci.* **7**, 231 (1958)
M. Jones *et al.*, *Phys. Rev. Lett.* **84**, 1398 (2000).

[2] I. Passchier *et al.*, *Phys. Rev. Lett.* **82**, 4988 (1999)
D. Rohe *et al.*, *Phys. Rev. Lett.* **83**, 4257 (1999).

[3] K. Aniol *et al.*, *Phys. Rev. Lett.* **82**, 1096 (1999)
D. Spayde *et al.*, *Phys. Rev. Lett.* **84**, 1106 (2000).

[4] J. Friedman ad H. Kendall, *Ann. Rev. Nucl. Sci.* **22**, 203 (1972).

[5] K. Abe *et al.*, *Phys. Lett.* **B364**, 61 (1995)
K. Abe *et al.*, *Phys. Rev. Lett.* **79**, 26 (1997)
P. Anthony *et al.*, *Phys. Lett.* **B463**, 339 (1999).

[6] D. Adams *et al.*, *Phys. Lett.* **B396**, 338 (1997)
D. Adams *et al.*, *Phys. Rev.* **D56**, 5330 (1997).

[7] M. Burkardt, *Phys. Rev.* **D62**, 071503 (2000)
J.P. Ralston and B. Pire, *Phys. Rev.* **D66**, 111501 (2002)
M. Diehl, *Eur. Phys. J.*, **C25**, 223 (2002)
A.V. Belitsky *et al.*, *Nucl. Phys.* **A711**, 118 (2002).

[8] S. Stepanyan *et al.*, *Phys. Rev. Lett.* **87**, 182002 (2001)
A. Airapetian *Phys. Rev. Lett.* **87**, 182001 (2001).

[9] P. Bertin, C.E. Hyde-Wright, R. Ransome and F. Sabatié, experiment E00-110. http://www.jlab.org/∼sabatie/dvcs.

[10] D. Müller *et al.*, *Fort. Phys.* **42**, 101 (1994)
A.V. Radyushkin, *Phys. Lett.* **B380**, 417 (1996)
A.V. Radyushkin, *Phys. Lett.* **B385**, 333 (1996)
X. Ji, *Phys. Rev.* **D55**, 7114 (1997)
J. Collins and A. Freund, *Phys. Rev.* **D59**, 074009 (1999).

[11] X. Ji, *Phys. Rev. Lett* **78**, 610 (1997).

[12] A.V. Belitsky, D. Muller and A. Kirchner, *Nucl. Phys.* **B629**, 323 (2002).

[13] S.J. Brodsky, F. Close, J.F. Gunion, *Phys. Rev.* **D6**, 177 (1972).

[14] M. Diehl *et al.*, *Phys. Lett.* **B411**, 183 (1997).

[15] Model following K. Goeke, M.V. Polyakov and M. Vanderhaeghen, *Prog. Part. Nucl. Phys.* **47**, 401 (2001) . Implementation by L. Mossé and adaptation to the neutron by F. Sabatié.

[16] Lacombe *et al.*, *Phys. Lett.* **101B**, 139 (1981)
M. Garçon and J.W. Van Orden, *Adv. Nucl. Phys.* **26**, 293 (2001).

[17] M. Vanderhaeghen and J.W. Van Orden, private communication.